Appl Phys B (2009) 94: 1–27
DOI 10.1007/s00340-008-3286-x

Applied Physics B
Lasers and Optics

INVITED PAPER

Continuous-wave cavity-ringdown detection of stimulated Raman gain spectra

F.V. Englich · Y. He · B.J. Orr

Received: 10 October 2008 / Published online: 15 November 2008

Abstract Cavity ringdown (CRD) spectroscopy, with its high sensitivity, provides a novel way to perform continuous-wave (cw) stimulated Raman gain (SRG) spectroscopy, rather than by conventional optically detected coherent Raman techniques. Tunable cw laser light at ∼1544 nm is used to probe ringdown decay from a rapidly-swept, high-finesse optical cavity containing a gas-phase sample of interest and itself located inside the cavity of a cw single-longitudinal-mode Nd:YAG ring laser operating at ∼1064.4 nm. This approach is used to measure cw SRG spectra of the ν_1 fundamental rovibrational Raman band of methane gas at $\sim 2916.5\ \text{cm}^{-1}$. The resulting SRG-CRD resonances have ringdown times longer than in the off-resonance case, in contrast to the usual shorter ringdown times arising from absorption and other loss processes. Previously reported noise-equivalent sensitivities have been substantially improved, by using a second ringdown cavity to facilitate subtraction of infrared-absorption background signals. Moreover, by employing a ringdown cavity in the form of a ring, the SRG-pump and CRD-detected Stokes beams can co-propagate uni-directionally, which significantly reduces Doppler broadening.

PACS 42.62.Fi · 42.65.Dr · 82.53.Kp

1 Introduction

It is well established that cavity ringdown (CRD) techniques, which examine the characteristic exponential decay of light from a high-finesse optical cavity, provide a useful way to record weak absorption spectra of gases, with high resolution and with high analytical sensitivity [1, 2]. An innovative form of continuous-wave (cw) CRD spectroscopy, in which its conventional optical-absorption mode of operation was extended for the first time into the regime of coherent Raman spectroscopy [3, 4], was reported in an earlier paper in this journal [5]. From another viewpoint, our cw SRG-CRD spectroscopic approach provides a novel means of performing cw stimulated Raman gain (SRG) spectroscopy, in contrast to more conventional optically detected forms of coherent Raman spectroscopy.

In this paper, we expand on our previous brief report on cw SRG-CRD spectroscopy [5] and provide a more detailed description of our experimental methodology, including techniques that have substantially enhanced the attainable noise-equivalent sensitivity and quality (e.g. Doppler-limited optical bandwidth) of the resulting cw SRG-CRD spectra [6, 7].

Introducing our approach [5, 6], Fig. 1 depicts our recently developed "ring-in-a-ring" cw SRG-CRD spectrometer [7]. In this instrument, the ringdown cavity is inside the cavity of a cw Nd:YAG ring laser (reflectors M_1–M_4, with diode-pumped laser amplifier head L_P GAIN and optical diode OD to ensure uni-directional operation) that provides the high-power SRG-pump radiation needed to drive the SRG process. The ringdown cavity is itself a four-mirror ring (reflectors M_5–M_8, rapidly swept by a piezoelectric translator PZT) that is enclosed in an evacuable gas-sample chamber (- - -). Forward-transmitted CRD signals with decay time τ are probed by a tunable cw diode laser L_S

F.V. Englich · Y. He · B.J. Orr (✉)
MQ Photonics Research Centre, Department of Physics,
Macquarie University, Sydney, NSW 2109, Australia
e-mail: borr@ics.mq.edu.au
Fax: +61-2-98508115

Present address:
F.V. Englich
Jet Propulsion Laboratory, California Institute of Technology,
MS 300-123, 4800 Oak Grove Drive, Pasadena, CA 91109, USA

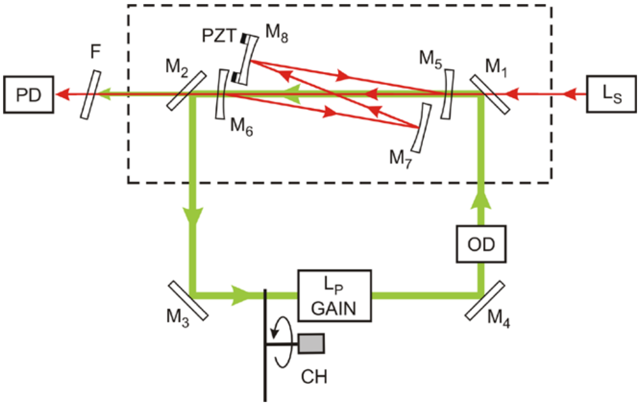

Fig. 1 Simplified layout of a "ring-in-a-ring" instrument for continuous-wave (cw) stimulated Raman gain/cavity ringdown (SRG-CRD) spectroscopy [6, 7]. Between mirrors M_5 and M_6, co-propagating coherent cw beams from the Nd:YAG pump laser (*broad line*) and the Stokes probe laser L_S (*fine line*) are co-focused and aligned to optimise their coherent Raman interaction. The cw SRG-CRD signal is monitored by photodetector PD, from which characteristic ringdown decay times τ can be extracted, as a measure of stimulated Raman gain. See text for further details

and photodetector PD, using a 1.06-μm filter F to protect PD from SRG-pump radiation. An optical chopper CH periodically blocks the Nd:YAG pump-laser cavity to allow subtraction of overlapping background absorption spectra. Broad and fine arrowed lines represent the path and direction of the Nd:YAG laser pump beam and the diode-laser Stokes (probe) beam, respectively, which are aligned to overlap efficiently inside the ringdown cavity between mirrors M_5 and M_6, as considered in Sect. 1.2 below. Details of such instrumentation and measurements are presented in Sects. 2–4. Meanwhile, we survey fundamental elements of our cw SRG-CRD approach in Sects. 1.1–1.3.

1.1 Stimulated Raman gain (SRG) spectroscopy: mechanistic fundamentals

The mechanistic basis of our cw SRG-CRD experiments is stimulated Raman scattering (SRS) from molecules in a gaseous sample that is irradiated by two beams of coherent light at pump and Stokes angular frequencies, ω_P and ω_S, respectively (where, by convention, $\omega_P > \omega_S$). For illustrative purposes, we consider the idealised plane-wave approximation, in which the corresponding electric field amplitudes of the two monochromatic traveling waves are $E_P(z,t)$ and $E_S(z,t)$, respectively, where z is the position along the propagation axis, t is the elapsed time, and the plane waves are taken to be linearly polarised in a common direction. The third-order nonlinear-optical coupling between these SRG-pump and Stokes waves gives rise to SRS (and also SRG) processes. In the slowly-varying envelope approximation, these processes are represented by a pair of scalar coupled-wave equations which are solutions to the nonlinear wave equation in the steady-state regime [8], as follows:

$$\frac{\partial}{\partial z}E_P = \frac{i3\omega_P^2}{4k_P c^2}\chi^{(3)}(-\omega_P;\omega_S,-\omega_S,\omega_P)|E_S|^2 \times E_P \exp(i\Delta k z), \tag{1}$$

$$\frac{\partial}{\partial z}E_S = \frac{i3\omega_S^2}{4k_S c^2}\chi^{(3)}(-\omega_S;\omega_P,-\omega_P,\omega_S)|E_P|^2 \times E_S \exp(i\Delta k z). \tag{2}$$

Here, $\chi^{(3)}(-\omega_P;\omega_S,-\omega_S,\omega_P)$ and $\chi^{(3)}(-\omega_S;\omega_P,-\omega_P,\omega_S)$ are the relevant nonlinear-optical susceptibilities, c is the speed of light, and $k_j = n_j\omega_j/c$ $(j = \mathrm{P}, \mathrm{S})$ are the respective SRG-pump and Stokes wave vectors for refractive indices n_j. It follows that the wave-vector mismatch factors Δk are necessarily zero, in view of the following relationships:

$$\Delta k = k_P - (k_S - k_S + k_P) = k_S - (k_P - k_P + k_S) = 0. \tag{3}$$

The SRS susceptibilities $\chi^{(3)}$ in (1) and (2) effectively couple the two radiation fields E_P and E_S, enabling transfer of optical energy between them. Here, we focus on SRG processes, which are typically measured with $|E_P| \gg |E_S|$ so that the net effect is transfer of optical energy *from* the radiation field at ω_P *to* that at ω_S, while the molecules are correspondingly Raman-excited. Equation (2) is then crucial in describing how a weak Stokes "probe" radiation field (E_S) is amplified along the z-axis through energy transfer from the SRG-pump radiation field (E_P), which has a much higher irradiance I_P than the Stokes probe.

A significant outcome of the zero value of Δk in (3) is that the so-called "non-parametric" SRS and SRG processes are intrinsically phase-matched, regardless of dispersion and other properties of the medium [8–10]. This absence of a critical phase-matching geometry means that SRS and SRG experiments can be performed with non-collinear pump and Stokes beams, thereby facilitating separation of the pump and Stokes beams [8]. However, the efficiency of SRG detection depends crucially on close spatial overlap of pump and Stokes beams over an extended path within the Raman gain medium, so that it is advantageous to use co- or counter-propagating Stokes and pump beams. Moreover, as we shall demonstrate in this paper, the co-propagating geometry provides a further advantage in that it helps to minimise the Doppler broadening of resulting gas-phase SRG spectra.

The functional form of an SRG process can be derived by solving (2) in the small-signal limit where pump-wave depletion is negligible. After traversing an interaction length L_R in the Raman-active medium, the irradiance I_S of the Stokes wave is found [8] to be:

$$I_S(L_R) = I_S^0 \exp(g_R I_P L_R) \approx \{I_S^0(1 + g_R I_P L_R)\}, \tag{4}$$

where I_{S}^{0} is the incident irradiance of the Stokes wave, I_{P} is the irradiance of the SRG-pump wave (assumed to be undepleted and therefore constant over the Raman-active medium), and the approximation $\{\ldots\}$ applies in the limit of low gain. The parameter g_{R} (the plane-wave Raman gain per unit pump irradiance) is proportional to the nonlinear-optical Raman susceptibility χ_{R} from (2); this can usefully separated into its real and imaginary parts:

$$\chi_{\mathrm{R}} = \chi^{(3)}(-\omega_{\mathrm{S}}; \omega_{\mathrm{P}}, -\omega_{\mathrm{P}}, \omega_{\mathrm{S}}) = \chi_{\mathrm{R}}' + i\chi_{\mathrm{R}}''. \tag{5}$$

In the special case where the difference $(\omega_{\mathrm{P}} - \omega_{\mathrm{S}})$ between SRG-pump and Stokes frequencies is in exact resonance with a Raman transition frequency Δ_{R} (i.e. satisfying the two-photon resonance condition, $\omega_{\mathrm{P}} - \omega_{\mathrm{S}} = \Delta_{\mathrm{R}}$), the nonlinear-optical Raman susceptibility χ_{R} is purely imaginary (i.e. $\chi_{\mathrm{R}}^{\mathrm{res}} = i\chi_{\mathrm{R}}''$). It is then found [8] that the "peak on-resonance" gain coefficient $g_{\mathrm{R}}^{\mathrm{res}}$ for a medium of interest is real and of the form:

$$g_{\mathrm{R}}^{\mathrm{res}} = g_{\mathrm{R}} = -\left(\frac{3\omega_{\mathrm{S}}}{\varepsilon_0 c^2 n_{\mathrm{S}} n_{\mathrm{P}}}\right)\chi_{\mathrm{R}}'', \tag{6}$$

where ε_0 is the electric permittivity of a vacuum. It should be noted that χ_{R}'' is intrinsically negative and the real part of g_{R} is necessarily positive. Equation (4) therefore describes exponential growth of the irradiance I_{S} as the Stokes wave traverses the Raman gain medium.

For SRS in molecular media, it is convenient to express g_{R} in terms of the differential Raman scattering cross-section $(\mathrm{d}\sigma_{\mathrm{R}}/\mathrm{d}\Omega)$, where Ω is the solid angle of collection, which is experimentally determined by measuring spontaneous Raman scattering for a spectroscopic feature of interest (e.g. a rovibrational Q branch in the case of gas-phase molecules). If we assume that g_{R} and $(\mathrm{d}\sigma_{\mathrm{R}}/\mathrm{d}\Omega)$ have a Lorentzian lineshape function with full-width-at-half-maximum (FWHM) linewidth $\Delta\omega_{\mathrm{R}}$ (as for gases at moderate pressures), (6) becomes [8]:

$$g_{\mathrm{R}}^{\mathrm{res}} = \left(\frac{4\lambda_{\mathrm{S}}^2 n_{\mathrm{S}}}{\hbar\omega_{\mathrm{P}} n_{\mathrm{P}}}\right)\Delta N \frac{1}{\Delta\omega_{\mathrm{R}}}\left(\frac{\mathrm{d}\sigma_{\mathrm{R}}}{\mathrm{d}\Omega}\right)\left(\frac{\omega_{\mathrm{P}} n_{\mathrm{S}}}{\omega_{\mathrm{S}} n_{\mathrm{P}}}\right), \tag{7}$$

where ΔN is the difference in number density between ground and excited molecular states, λ_{S} is the wavelength of Stokes light, and $\hbar$ $(= h/2\pi)$ is the reduced form of Planck's constant h. It should be noted that $(\mathrm{d}\sigma_{\mathrm{R}}/\mathrm{d}\Omega)$ in (7) is defined in terms of the ratio of scattered and incident *optical power* or *irradiance* and that the factor $(\omega_{\mathrm{P}} n_{\mathrm{S}}/\omega_{\mathrm{S}} n_{\mathrm{P}})$ effectively converts it to a differential Raman scattering cross-section in terms of *photon numbers* [12, 13], as is used in [8]. Equation (7) differs trivially by a factor of $(n_{\mathrm{S}} n_{\mathrm{P}})^{-1}$ from a similar result in [11].

A convenient alternative form of (7) is obtained by replacing angular-frequency quantities (ω_{P} and $\Delta\omega_{\mathrm{R}}$) and the wavelength λ_{S} by their optical-frequency equivalents (ν_{P}, $\Delta\nu_{\mathrm{R}}$, and ν_{S}, respectively, in Hz units), as follows [8]:

$$g_{\mathrm{R}}^{\mathrm{res}} = \left(\frac{2c^2}{\pi h \nu_{\mathrm{S}}^3 n_{\mathrm{P}}^2}\right)\Delta N \frac{1}{\Delta\nu_{\mathrm{R}}}\left(\frac{\mathrm{d}\sigma_{\mathrm{R}}}{\mathrm{d}\Omega}\right). \tag{8}$$

Apparent discrepancies between relationships equivalent to (7) and (8) (for instance, in [14–18]) can be resolved on the basis of the two forms of $(\mathrm{d}\sigma_{\mathrm{R}}/\mathrm{d}\Omega)$, in terms of *either* number of photons *or* of irradiance, as explained in the context of (7) above. There are also assorted inconsistencies in refractive-index factors (including use of an averaged value n in place of n_{P} and n_{S} [14, 15]).

Typical molecular rovibrational Raman scattering cross-sections $(\mathrm{d}\sigma_{\mathrm{R}}/\mathrm{d}\Omega)$ are of the order of 10^{-31} cm^2 sr^{-1} molecule^{-1} [17], yielding a spontaneous Raman scattering signal that is weak relative to Rayleigh scattering and stray light. As a coherent Raman-spectroscopic technique using a strong SRG-pump laser beam to excite the molecules of interest, SRG offers several practical advantages over spontaneous Raman spectroscopy, namely [4, 19, 20]:

- The Stokes (probe) SRG output signal, carried on a coherent laser-like beam, can be spectrally and spatially separated from interfering background luminescence.
- As for other coherent Raman techniques such as coherent anti-Stokes Raman spectroscopy (CARS) [21], inverse Raman spectroscopy (IRS) [22], photoacoustic Raman spectroscopy (PARS) [23], the resolving power of SRG spectroscopy is high, limited ultimately by the optical bandwidth of the laser sources used and not by the resolution of a spectrophotometer (typically ~0.1 cm^{-1}) as in spontaneous Raman spectroscopy.
- Unlike parametric nonlinear-optical processes such as CARS [21], SRG and SRS are non-parametric processes and therefore intrinsically phase-matched, as discussed in the context of (3) above.
- Also in contrast to CARS with its complicated dependence on $|\chi^{\mathrm{CARS}}|^2$ (where χ^{CARS} is a combination of nonresonant and complex resonant nonlinear-optical susceptibilities) and on the product $I_{\mathrm{P}}^2 I_{\mathrm{S}}$ of pump and Stokes irradiances [21], the peak amplitudes in SRG spectra have a simple linear dependence on the imaginary part of χ_{R} and on the irradiance $\mathcal{I}_{\mathrm{P}}$ of the pump beam, as in (4)–(6) above. Relative to CARS, SRS-based techniques such as SRG spectroscopy can therefore be significantly more sensitive and less degraded by nonresonant background effects, so that they are amenable to measurement with low-power cw laser sources [19].

The foregoing plane-wave approximation characterises key mechanistic elements of SRG spectroscopy. However, it provides only a simplistic description of actual SRG experiments where the pump and Stokes (probe) beams are focused in order to enhance the Raman gain factor ($g_R\ I_P\ L_R$) of (4), by increasing the pump irradiance I_P and optimally matching the overlap of co-focused pump and Stokes waves. It is more appropriate to represent the spatial variation of the irradiances I_P and I_S in terms of confocal single-longitudinal-mode (SLM) TEM$_{00}$ Gaussian beams, both along the propagation axis z and transversely (x, y) [11, 12, 24]. After integrating ($g_R\ I_P\ L_R$) over these spatial variations, (4) is replaced by the following expression for the single-pass power gain of the Stokes beam:

$$P_S(L_R) = P_S^0 \exp(\langle g_R I_P L_R \rangle) \approx \{P_S^0(1 + \langle g_R I_P L_R \rangle)\}, \quad (9)$$

where P_S^0 is the incident power of the Stokes (probe) beam as it enters the zone in which it can interact with the pump beam and $P_S(L_R)$ is the power of the Stokes beam after traversing that zone, of length L_R. As before, the approximation $\{\dots\}$ applies in the limit of low gain. The integrated Raman power-gain factor $\langle g_R\ I_P\ L_R \rangle$ for the Stokes (probe) beam, depending on L_R and the spatially varying irradiance I_P of the SRG-pump beam, is related to the plane-wave Raman gain coefficient g_R as follows [11]:

$$\langle g_R I_P L_R \rangle = 4 P_P g_R (\lambda_P + \lambda_S)^{-1} \tan^{-1}(L_R/b), \quad (10)$$

where P_P is the pump-beam power (assumed to be undepleted and therefore constant) and $b = 2\pi\omega_P^2/\lambda_P$ is the confocal parameter (with wavelength λ_P and focal beam waist ω_P). Equation (10) describes the maximum attainable power-gain factor, with an optimal Stokes spot size (beam waist ω_S), chosen such that the two beams have the same confocal parameter, that is,

$$\omega_S/\omega_P = (\lambda_S/\lambda_P)^{1/2}. \quad (11)$$

Note that the focal beam waists ω_P and ω_S correspond to e^{-2} points of the transverse Gaussian power distributions (and to e^{-1} points of the transverse Gaussian electric-field distributions). Simulated overlapping beam geometries, that are attainable within the ringdown cavity of our actual cw SRG-CRD instruments, are considered in Sect. 1.2 below.

The Raman gain parameter g_R (units: $\mathrm{m\,W^{-1}}$), as in (4) and (6)–(8), is a bulk (intensive) property of the medium, which applies as well to spatially varying beams based on the power P, i.e. radiant flux (W), as it does to the plane-wave description in terms of irradiance I, i.e. radiant flux density ($\mathrm{W\,m^{-2}}$). On this basis, the plane-wave expression for the peak on-resonance Raman gain factor can then be converted to its optimal focused Gaussian-beam equivalent $\langle g_R^{\mathrm{res}}\ I_P\ L_R \rangle$ [11, 12, 24] simply by substituting g_R, as in (7) or (8), into (10).

1.2 SRG-CRD spectroscopy: cavity-ringdown detection of SRG spectra

As already implied in the context of (6) and (7) above, spectroscopic features occur in the SRG output from molecules of interest as a result of two-photon Raman resonances at difference frequencies $\Delta_R = (\omega_P - \omega_S)$ in their nonlinear-optical Raman susceptibility $\chi_R = \chi^{(3)}(-\omega_S; \omega_P, -\omega_P, \omega_S)$. SRG spectra are usually recorded by scanning either ω_P or ω_S and detecting changes in the power of the Stokes output light, which propagates as a coherent beam [3, 4]. However, in our novel CRD variant of SRG spectroscopy [5], we detect instead the I_P-dependent part of the ringdown decay time τ for the Stokes (probe) light, by tuning ω_S while holding ω_P fixed. Our results have been obtained by locating the sample of interest inside the optical cavity of a cw Nd:YAG ring laser as well as of the ringdown cavity, which may be linear (as in [5]) or ring-form (as in Fig. 1 above [6, 7]).

We adopt a distinctive rapidly-swept approach to cw CRD spectroscopy, which detects light *either* forward-propagating and directly transmitted by the ringdown cavity [25–28] *or* backward-propagating and reflected in optical-heterodyne (OH) mode from the ringdown cavity [26–28]. Our fully cw approach to SRG-CRD measurements, with continuous-wave pump and Stokes sources at ω_P and ω_S, has various advantages, including:

- The need to sustain the SRG process for the duration of the ringdown decay by means of a source of coherent pump radiation at ω_P that is cw (or at least quasi-cw with a pulse duration exceeding the ringdown time τ by more than an order of magnitude).
- The availability of compact, stable, narrowband cw tunable diode lasers for CRD probing at ω_S with the possibility of optimising CRD build-up times and duty cycles.
- The instrumental simplicity and efficacy of our rapidly-swept cw CRD approach [25–28], which avoids the need for an electro- or acousto-optic switch or for active control of the cavity's resonance condition.

A phenomenological plane-wave representation of such nonlinear-optical cw SRG-CRD experiments at a tunable Stokes frequency ω_S, in terms of the difference between the measured ringdown time τ and the empty-cavity ringdown time τ_0, is as follows [5]:

$$\tau^{-1}(\omega_S; \omega_P, I_P) = \tau_0^{-1} + \alpha(\omega_S)c - g_R(\omega_S, \omega_P) I_P (L_R/L_C) c, \quad (12)$$

where the coefficient $\alpha(\omega_S)$ is due to optical loss (e.g. absorption and scattering). The term containing ($g_R\ I_P$) is due to nonlinear-optical gain (i.e. SRG) that arises predominantly from (2) and causes the ringdown rate τ^{-1} to depend on ω_P and I_P as well as ω_S. Peak on-resonance values of the gain term in (12) depend [8] on the imaginary part χ_R'' of the nonlinear-optical susceptibility $\chi^{(3)}(-\omega_S; \omega_P, -\omega_P, \omega_S)$, as in the context of (5) and (6) above. Equation (12) includes a factor (L_R/L_C), comprising the ratio of the path length L_R in the Raman-active medium to the overall length L_C of the ringdown cavity. For a linear ringdown cavity (as in [5]) $L_R/L_C = 1$, but in the case of a ring-form ringdown cavity (as in Fig. 1 above) $L_R/L_C < 1$ since I_P is effectively zero in the portion of the ringdown cavity that does not lie within the SRG-pump laser cavity.

While a simplistic plane-wave description, as in (12), is phenomenologically instructive, it fails to describe the actual spatial profiles of the overlapping SRG-pump and Stokes (probe) beams. The spatial mode profile of the Stokes beam inside the ringdown cavity is determined by the geometry and mirrors of the ringdown cavity itself, and needs to be matched, as in the context of (11), to the overlapping spatial mode profile of the SRG-pump beam, which also depends on intracavity elements of the Nd:YAG ring laser and its thermal lensing effects (as outlined in Sect. 2.1 below). To ensure close spatial overlap of the two co- and/or counter-propagating beams, our cw SRG-CRD instrument optimisation has entailed detailed simulation of mode profiles, as discussed in Sects. 2–4 below. For instance, Table 1 summarises the outcome of such beam-overlap simulations [6], for two distinct forms of cw SRG-CRD spectrometer, that will be further considered in Sects. 2–4.

It should also be noted that the effective coefficients $\alpha(\omega_S)$ and $g_R(\omega_S, \omega_P)I_P$ in (12) need to be averaged over the single-pass optical paths (L_C and L_R, respectively) through the sample in the ringdown cavity; for instance, Raman gain with confocal Gaussian SRG-pump and Stokes beams has been considered in the context of (9)–(11) above.

As previously reported [5], the fact that SRG is a gain process for the Stokes (probe) radiation rather than a loss process results in an apparent peculiarity that distinguishes CRD processes associated with SRG from the usual loss-related CRD processes. This remarkable distinction is evident in the opposite signs of the loss and gain terms in (12). When the difference frequency $(\omega_P - \omega_S)$ is tuned to a Raman resonance at Δ_R, the former $\alpha(\omega_S)$-dependent term yields a *decreased* ringdown time τ (as is typical in CRD absorption spectroscopy). However, the latter $(g_R\, I_P)$-dependent term results in a *prolonged* ringdown time τ (and thus a reduced CRD decay rate τ^{-1}), simply because it corresponds to optical gain.

This latter outcome, resulting in CRD-spectroscopic resonances with prolonged values of ringdown time τ, is unfamiliar in the regular CRD context because it usually pertains to optical loss processes (such as absorption, scattering, and imperfect mirror reflectivity) rather than to gain processes (e.g. as in the case of SRG). Nevertheless, it should be noted that the SRG-CRD situation has a consistent relationship to cw operation of a Raman laser oscillator [15, 16, 18]. In a cw Raman laser, a resonant optical cavity encloses a Raman gain medium which may be a gas [29–37], a liquid [38–41], a bulk crystalline solid (either insulating [42–46] or semiconducting [47, 48]), an optical fiber [49, 50], or a whispering-gallery-mode (WGM) microresonator [39–41, 51–55]. As the oscillation threshold of a Raman laser is approached, the irradiance I_S of the Stokes wave increases, becoming comparable to I_P, and the coupling between (1) and (2) becomes more pronounced than for SRG with relatively low I_S. The effective CRD decay rate τ^{-1} for the Stokes radiation is then markedly reduced; a cw Raman laser therefore corresponds to the extreme (high-I_P) limiting case of SRG-CRD, where τ^{-1} is typically [5–7] only slightly less than τ_0^{-1} at lower I_P.

Comparable CRD effects have recently been observed [56] as a result of SRS in a CaF_2-disk WGM resonator (4-mm radius, 8.2-GHz free spectral range, 322-cm^{-1} Δ_R; Q factor of $> 10^9$). This device was pumped quasi-continuously by rectangular pulses from a 1.32-μm Nd:YAG laser ($\sim$60 mW incident power, 4-kHz optical bandwidth) and the exiting pump light exhibited a nonexponential ringdown decay with two characteristic CRD decay times: $\tau_{\text{fast}} \approx 6.5$ μs and $\tau_{\text{slow}} \approx 26$ μs, corresponding to $Q \approx \sim 9 \times 10^9$ and $Q \approx \sim 4 \times 10^{10}$, respectively. On the basis of a corresponding model [57] the fast and slow decays were attributed to operation above and below the SRS threshold, respectively, and their factor of 4 difference enabled SRS gain and threshold parameters of the resonator to be deduced.

1.3 Spectroscopic preliminaries for the molecule of interest: methane ($^{12}CH_4$)

1.3.1 Relevant infrared and Raman spectra of CH_4 *gas*

Methane (CH_4) has gained prominence as a standard test molecule in the development of various forms of high-resolution coherent Raman spectroscopy [4, 19–23, 58–63]. In particular, the ν_1 fundamental rovibrational Raman band of $^{12}CH_4$ gas, the Q-branch peak of which is at $\Delta_R = 2916.7$ cm^{-1}, has been widely investigated by high-resolution spontaneous Raman spectroscopy [64, 65], SRS (i.e. SRG and/or inverse Raman) spectroscopy [4, 20, 66–74], and CARS spectroscopy [71, 75–81]. High-resolution SRS spectroscopy has also been applied to the corresponding ν_1-band Q branch of other tetrahedral isotopomers of methane: $^{13}CH_4$ [68, 82], $^{12}CD_4$ [68, 83, 84], $^{13}CD_4$ [85].

The same Q branch in the ν_1 Raman band of $^{12}CH_4$ gas has been used to demonstrate the feasibility of our cw SRG-CRD approach [5–7] and is further explored in this paper. The predominant contribution to all such SRG-CRD spectra arises inevitably from a background of CRD linear absorption spectrum of $^{12}CH_4$. Such a spectrum has been documented without quantum assignment in the HITRAN 2004 spectroscopic database [86, 87] (after work on this project had commenced [6]) and is illustrated in Fig. 2. By using SRG-pump radiation from a Nd:YAG laser at $\lambda_P \approx 1064.4$ nm, the peak of the $^{12}CH_4$ ν_1-band Q branch at

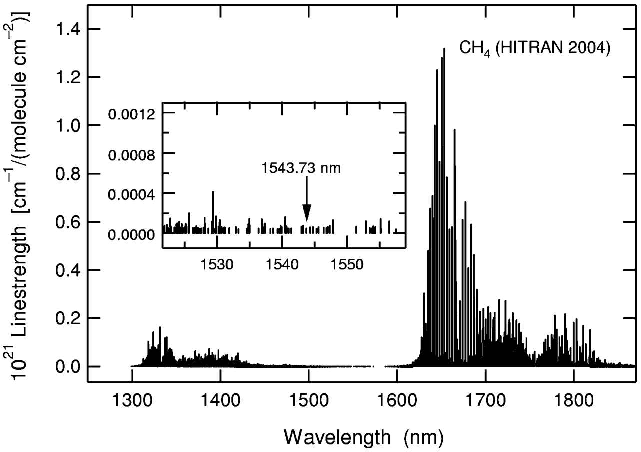

Fig. 2 Predicted stick spectrum for linear absorption by $^{12}CH_4$ gas, based on the HITRAN 2004 spectroscopic database [86, 87]. The *arrow* in the inset designates a relatively weak (but still significant) absorption peak at a wavelength of 1543.73 nm. This coincides with tunable Stokes wavelengths λ_S needed to probe the 2916.7-cm^{-1} Q branch in the ν_1 Raman band of $^{12}CH_4$ when using a Nd:YAG pump laser with wavelength $\lambda_P \approx 1064.4$ nm to record cw SRG-CRD spectra

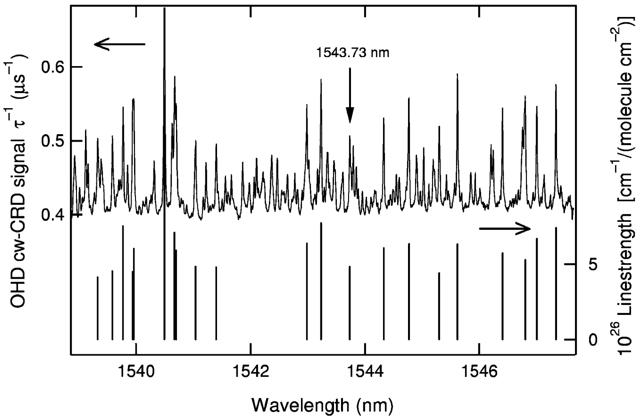

Fig. 3 *Upper trace*: observed absorption spectrum of $^{12}CH_4$ gas (pressure $p = 250$ Torr, temperature $T = 300$ K), recorded by swept-frequency cw CRD spectroscopy [88, 89] in the backward-propagating optical-heterodyne mode of detection [26, 27]; the cw CRD spectrum (~2290 data points, covering wavelengths from 1538.86 nm to 1547.65 nm) is a wide-ranging average of 400 successively recorded spectra acquired at a rate of 2 Hz by means of a swept-frequency cw diode laser (iolon SLE1040). *Lower trace*: predicted stick spectrum for absorption by $^{12}CH_4$ gas, based on the HITRAN 2004 spectroscopic database [86, 87]. As in Fig. 2, the prominent absorption peak at 1543.73 nm (6477.8 cm^{-1}) in the region of primary interest is designated with an *arrow*

$\Delta_R \approx 2916.7$ cm^{-1} corresponds to a SRG Stokes wavelength $\lambda_S \approx 1543.6$ nm. As shown in Fig. 2, this coincides with an apparent "window" in the linear absorption spectrum of $^{12}CH_4$. However, although such absorption is extremely weak in this spectral region, it is far from negligible, overlapping and tending to mask the (even weaker) SRG-CRD spectrum of interest. In this region, the prominent absorption feature at 1543.73 nm (arrowed in Fig. 2), has been found to contribute much more to CRD τ^{-1} values than the SRG signals that can realistically be generated in our SRG-CRD approach. It has therefore been necessary to implement elaborate background-subtraction strategies to extract the SRG spectra of interest [5–7].

This part of the absorption spectrum of $^{12}CH_4$ gas (pressure $p = 250$ Torr, temperature $T = 300$ K), has been measured by swept-frequency cw CRD spectroscopy [88, 89], recorded in the backward-propagating OH-detected mode [26, 27]. The resulting cw CRD spectrum, shown in the upper trace of Fig. 3, comprises ~2290 data points, averaged over 400 successive rapid (2-Hz) frequency sweeps covering a wide wavelength range (1538.86–1547.65 nm, corresponding to 6498.3–6461.4 cm^{-1}). The linear CRD absorption cell ($L_C \approx 30$ cm, with $>99.96\%$ mirror reflectivity at ~1550 nm; see Sect. 3 below for details) is probed by light from a swept-frequency tunable diode laser (iolon, model SLE1040). This laser, a miniature (50 ×70 × 13 mm) external-cavity system (with Littman–Metcalf architecture, a reference étalon for internal wavelength calibration, and integrated control electronics), is based on microelectromechanical-systems (MEMS) technology [90]; its fibre-coupled output power is ~10 mW, with an intrinsic optical bandwidth $\Delta\nu_L = 125$ kHz, a frequency stability of ~1 MHz over ~3.5 µs, and monochromatic output that can be continuously swept without mode hops over its entire tuning range of ~8 THz from 1.51 to 1.57 µm at an optical-frequency (or wavelength) sweep rate of 1.25–125 THz s^{-1} (or 0.01–1.0 µm s^{-1}) and a repetition-rate range of 0.125–100 Hz. The output and synchronisation of data collection for the MEMS-based tunable laser is controlled via a computerised interface (see Sect. 2.2 for details). With the free spectral range (FSR) of the ringdown cavity effectively defining a sampling grid to measure absorbance-dependent ringdown times τ at successive cavity-resonance frequencies [88, 89], it is possible to generate an extensive, wide-ranging cw CRD absorption spectrum at a high data rate within a single rapid sweep cycle of the tunable diode laser. An analog detection scheme [89] generates OH-detected cw CRD signal output as a voltage that is proportional to the ringdown time τ.

The lower trace in Fig. 3 is a predicted partial absorption spectrum for $^{12}CH_4$ gas, based on the HITRAN 2004 spectroscopic database [86, 87]; it is well matched by much of the observed cw CRD spectrum in the upper trace, which has a FWHM pressure-broadened linewidth of ~0.025 nm. As in Fig. 2, the prominent 1543.73-nm (6477.8-cm^{-1}) absorption peak, with a linestrength $S = 4.85 \times 10^{-26}$ cm^{-1}/(molecule cm^{-2}), is designated with an arrow. Under these experimental conditions, this linestrength corresponds to a linear absorption coefficient of $\sim 2.4 \times 10^{-6}$ cm^{-1} and a CRD decay-rate increment $(\tau^{-1} - \tau_0^{-1})$ of ~0.08 µs^{-1}, which is consistent with our CRD measurements of τ^{-1} for this and other HITRAN 2004 absorption features in the vicinity of 1.54 μm [86].

Incidentally, we note two recent detailed studies of diode-laser absorption spectra of $^{12}CH_4$ gas in the vicinity of interest: line-intensity measurements from long-path absorption spectra in the range of 1509–1513 nm (6625–6608 cm^{-1}) [91] and cw CRD spectroscopy between 1500 and 1600 nm [92], but concentrating primarily on 1530–1539 nm (6535–6498 cm^{-1})—just beyond the range examined in Fig. 2.

1.3.2 Prediction of SRG-CRD spectra of CH_4 *gas*

In order to predict the magnitude of cw SRG-CRD spectra of interest, we need to consider a number of contributing factors. These are as follows for the 2916.7-cm^{-1} fundamental ν_1-band Q branch of $^{12}CH_4$ gas, under the same experimental conditions as in Fig. 3 (i.e. with $p = 250$ Torr and $T = 300$ K in a linear ringdown cell with $L_C = L_R = 30$ cm):

- The relevant Raman scattering cross-section $(d\sigma_R/d\Omega)$, as in (7) and (8), has been reported on several occasions [13, 65, 93]; we use the average value of 8×10^{-32} $cm^2\,sr^{-1}\,molecule^{-1}$ for $\lambda_P = 1064$ nm [13]. As explained in the context of (7) above, this value of $(d\sigma_R/d\Omega)$ is defined in terms of optical power or irradiance (rather than in terms of photon numbers).
- The effective FWHM linewidth $\Delta\nu_R$, as in (8), has been measured by inverse Raman spectroscopy as a linear function of pressure in the range from 1 to 50 atm for the Raman spectrum of interest [13, 94, 95] and extrapolates to ∼9 GHz (∼0.3 cm^{-1}) in the limit of lower pressures ($p < 760$ Torr). This Raman linewidth applies to the overall ν_1-band contour, as in the case of the above value of $(d\sigma_R/d\Omega)$ [13], rather than to more finely resolved rovibrational features. It is therefore appropriate to adopt $\Delta\nu_R = 9$ GHz (0.3 cm^{-1}) to obtain a spectrally averaged estimate of g_R^{res}, using (8).

In this SRG-CRD context, it is relevant to define the effective noise-equivalent sensitivity in terms of a "minimum detectable loss or gain" (MDLG) value; this is a generalised counterpart of the "minimum detectable absorption loss" (MDAL) used in regular CRD absorption spectroscopy [1]. Likewise, we define a data-rate-normalised value as $MDLG_N = MDLG\ N^{-1/2}$, where N is the number of data-point measurements per second. Our previously reported cw SRG-CRD-spectroscopic experiments [5] have yielded $MDLG = 1.6 \times 10^{-8}$ cm^{-1} (normalised to $MDLG_N = 5 \times 10^{-8}$ $cm^{-1}\,Hz^{-1/2}$ for CRD detection at 9 s per data point) for the 1544-nm Stokes beam; this is ∼750 times less than the linear absorption coefficient of $\sim 1.2 \times 10^{-5}$ cm^{-1} for the 1543.73-nm (6477.8-cm^{-1}) feature under the conditions of Fig. 3. In order to attain cw SRG-CRD spectra of acceptable quality this MDLG value needs to be exceeded by a factor of at least 10. Within the simplistic plane-wave approximation, as in (7), (8), and (12), the above value of g_R^{res} enables us to estimate that a desirable MDLG value of 1.6 $\times 10^{-7}$ cm^{-1} would be attained with an effective (spatially averaged) pump irradiance $I_P = 190$ $W\,mm^{-2}$. By crudely adapting the focused Gaussian beam model, as outlined in (9)–(11), we can equate this I_P-dependent sensitivity to $\langle g_R I_P L_R \rangle / L_C$, where $L_R = L_C$ for a linear ringdown cavity.

We have previously shown [5] that cw SRG-CRD spectra with spatially averaged pump irradiances of at least 200 $W\,mm^{-2}$ can be measured by overlapping optimally focused SRG-pump and Stokes beams in a ringdown cavity that is itself inside the ring cavity of a cw Nd:YAG pump laser. However, the corresponding SRG-CRD signal sensitivity (1.6 $\times 10^{-7}$ cm^{-1}) and CRD decay-rate increment $(\tau^{-1} - \tau_0^{-1}) = 0.0048$ μs^{-1} are still a factor of ∼75 smaller than those for the typical 1543.73-nm (6477.8-cm^{-1}) absorption feature, so that detection of cw SRG-CRD spectra necessitates elaborate background-subtraction measures [5].

Apart from predicting the magnitude of cw SRG-CRD spectra (relative to intrinsic noise and background absorption, as above) we need also to generate realistic rovibrational band contours for a variety of sample pressures and beam configurations (i.e. whether the SRG-pump and Stokes beams are co-propagating, counter-propagating, or both). This is necessary to test the reliability and quality of our intracavity-pumped cw SRG-CRD spectra. Our SRG-CRD band-contour model incorporates Voigt spectral profiles for individual rovibrational features in such spectra with a Lorentzian collisional linewidth $\Delta\nu_C$ and a Gaussian Doppler linewidth $\Delta\nu_D$ (both FWHM). These are combined with flexible fitting parameters and the best-available rovibrational line spectra, as has previously been briefly reported [5].

A key resource in this context is a set of measured and simulated cw SRG spectra that have been reported by Owyoung and co-workers [20, 66, 67]. For example, one of the icons of coherent Raman spectroscopy is a high-resolution cw SRG spectrum, for the 2916.7-cm^{-1} ν_1-band Q branch of $^{12}CH_4$ gas at $p = 35$ Torr and 297 K, published in several places (e.g. Fig. 16 of [20], Fig. 4.14 of [60], Fig. 2 of [66, 67], and Fig. 2 of [70]). Nevertheless, it has subsequently been recognised [80, 81, 96–99] that there are discrepancies (e.g. for Q-branch features with $J = 4$–6 in the Raman-shift frequency range of 2916.70–2916.75 cm^{-1}) between the set of calculated line frequencies with spectroscopic transition assignments and the cw SRG spectrum experimentally recorded at $p = 35$ Torr [66, 67], particularly for Q-branch features with $J = 4$–6 in the Raman-shift frequency range of 2916.70–2916.75 cm^{-1}.

To address this problem of constructing dependable rovibrational band contours for our SRG-CRD spectra, we started with the comprehensive model of Santos et al. [73], based on the line frequencies and relative peak heights measured in a low-temperature ($T = 77$ K, $p = 10$ Torr) quasi-cw SRS spectrum of the 2916.7-cm^{-1} Q branch in the ν_1 band of $^{12}\text{CH}_4$ gas. With $\Delta\nu_\text{D}$ set at 0.19 GHz (0.0063 cm^{-1}) and $\Delta\nu_\text{C} = 0$, we obtain a satisfactory fit to the SRS spectrum of Santos et al. [73]. However, there are still discrepancies when this model is used, with $\Delta\nu_\text{D} = 0.27$ GHz (0.009 cm^{-1}) and various $\Delta\nu_\text{C}$ values around $\Delta\nu_\text{C} = 0.15$ GHz (0.005 cm^{-1}), to predict the band contour of the 35-Torr, 297-K cw SRG spectrum observed by Owyoung and co-workers [66, 67]. We therefore resolved to combine their seemingly reliable calculated relative peak heights [66, 67] with the revised set of line frequencies deduced from CARS spectra by Lolck [81]. Our approach takes note of the fundamental distinction between rovibrational band contours for CARS spectra (which include interfering contributions from the real and imaginary parts of the nonlinear-optical Raman susceptibility χ_R [80]) and for SRG spectra (where peak amplitudes depend solely on the imaginary part of χ_R), as explained in the context of (5) and (6) above. This approach has been used to simulate Owyoung's SRG spectra [66, 67], using a Voigt profile with a Gaussian contribution of $\Delta\nu_\text{D} = 0.27$ GHz (0.009 cm^{-1}), corresponding to $T = 297$ K, and several trial collision-induced Lorentzian contributions ranging from $\Delta\nu_\text{C} = 0.12$ GHz (0.004 cm^{-1}) to $\Delta\nu_\text{C} = 0.21$ GHz (0.007 cm^{-1}), applicable in the vicinity of $p = 35$ Torr. The most satisfactory fit to the observed high-resolution 35-Torr SRG spectrum [66, 67] is obtained with $\Delta\nu_\text{C} = 0.15$ GHz (0.005 cm^{-1}).

Collision-induced Lorentzian contributions for SRG spectra at higher pressures p (Torr), as in Fig. 15 of [20] or Fig. 4 of [5], can then be derived by linear scaling of the above value of $\Delta\nu_\text{C}$ by a dimensionless factor of $(p/35)$; for instance, this yields a FWHM collisional linewidth $\Delta\nu_\text{C} = 1.05$ GHz (0.035 cm^{-1}) when $p = 250$ Torr [5]. Overall Voigt profiles, for SRG-CRD spectra of $^{12}\text{CH}_4$ gas at $T \approx 300$ K, are obtained by using FWHM Gaussian Doppler linewidths $\Delta\nu_\text{D}$ of 0.27 GHz (0.009 cm^{-1}) and/or 1.47 GHz (0.049 cm^{-1}); these correspond respectively to co- and counter-propagating SRG-pump and Stokes beams, and need to be appropriately chosen in the case of a uni-directional "ring-in-a-ring" configuration (as in Fig. 1) or combined as a 1:1 superposition in the case of a bi-directional linear ringdown cavity [5]. Such procedures were used in our previously reported simulation of a cw SRG-CRD spectrum at $p = 250$ Torr [5] and are further applied in Sects. 3 and 4.

Finally, it should be noted that the most adequate description of low-pressure SRG spectra, where individual rovibrational Raman features are discernible, is in terms of a spectroscopically resolved differential Raman scattering cross-section $(\text{d}^2\sigma_\text{R}/\text{d}\Omega\text{d}\nu_\text{S})$ (units: $\text{cm}^2\,\text{Hz}^{-1}\,\text{sr}^{-1}$ molecule^{-1}) [8–10, 20, 60, 68] combined with an appropriately structured spectral contour function, rather than the customary spectroscopically integrated differential Raman scattering cross-section $(\text{d}\sigma_\text{R}/\text{d}\Omega)$ (units: $\text{cm}^2\,\text{sr}^{-1}$ molecule^{-1}) combined with a linewidth factor $\Delta\nu_\text{R}{}^{-1}$ for the overall Raman band as in (8). We expect the latter approximation involving $(\text{d}\sigma_\text{R}/\text{d}\Omega)$ to be more truly applicable to SRG spectra recorded with $p \geq 150$ Torr than to higher-resolution SRG spectra (e.g. at 35 Torr and 75 Torr [20, 66, 67]).

1.4 SRG-CRD spectroscopy: overview of instrumentation and methodology

Details of the instrumentation and methodology for cw SRG-CRD spectroscopy are presented in Sects. 2, 3, 4 below, together with experimental results and related modeling.

In Sect. 2, we discuss the design and performance of a 1064-nm SLM cw noise-limited sensitivities (MDLG = 1.3×10^{-8} cm^{-1} and $\text{MDLG}_N = 2.6 \times 10^{-8}$ $\text{cm}^{-1}\,\text{Hz}^{-1/2}$, Nd:YAG ring laser [5, 6] that is the high-power pump laser source for various forms of intracavity-pumped cw SRG-CRD spectrometer; it has been depicted in Fig. 1 above.

Section 3.1 deals with Doppler-limited bi-directional cw SRG-CRD detection using a single intracavity linear ringdown cavity, as previously described in a brief preliminary paper [5]. A similar higher-performance cw SRG-CRD instrument, in which a second reference ringdown cavity is added to enhance the data rate, is presented in Sect. 3.2.

In Sect. 4, we discuss experiments that employ a uni-directional cw SRG-CRD spectrometer, as already illustrated schematically in Fig. 1 above and projected in our earlier paper [5]. This approach enables reduction of Doppler-broadened linewidths for higher SRG-CRD spectroscopic resolution, as introduced in Sects. 1.1 and 1.2 above.

These various forms of cw SRG-CRD spectrometer have been used to record SRG spectra of the ν_1 fundamental rovibrational Raman band of $^{12}\text{CH}_4$ gas at $\sim$2916.5 cm^{-1}, as introduced in Sect. 1.3 above and discussed in detail in Sects. 2–5 below.

2 Ring-cavity cw pump laser for intracavity SRG-CRD spectroscopy

2.1 Design and construction

The experimental configuration of a 1064-nm SLM cw Nd:YAG ring laser, specially designed as the pump laser source for our intracavity-pumped cw SRG-CRD spectrometers, is depicted in Fig. 4. The uni-directional ring laser resonator comprises four flat mirrors M_1–M_4 with high reflectivity ($R > 98\%$) at $\lambda_\text{P} = 1064$ nm and high optical transmission ($T_\text{opt} > 90\%$) at $\lambda_\text{S} \approx 1550$ nm. The round-trip

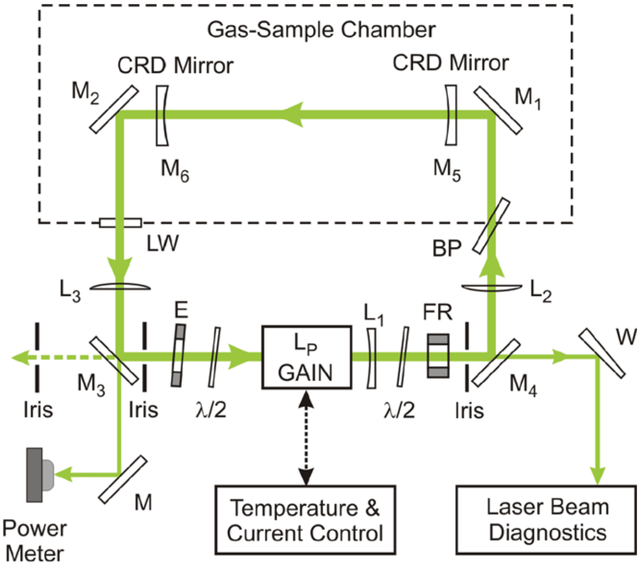

Fig. 4 Layout of a 1064-nm SLM cw Nd:YAG ring laser, comprising a uni-directional four-mirror resonator (M_1–M_4) based on a diode-pumped amplifier head (L_P GAIN), with intracavity linear ringdown cavity (M_5–M_6, inside an evacuable gas-sample chamber), optical diode (BP, FR, $\lambda/2$), second $\lambda/2$ plate to correct for thermal birefringence effects, étalon, and beam-shaping lenses (L_1–L_3). See text for further details

length of the laser resonator is ~1.41 m. No output coupler is used, in order to maximise intracavity laser power levels available for the intracavity cw SRG-CRD experiments. The gain medium of this SRG-pump laser (L_P GAIN) comprises a pre-aligned Nd:YAG amplifier head, radially pumped by three diode arrays (Cutting Edge Optronics, model RB-33) [6]; it is specified to deliver a typical multi-mode cw output power of 50 W at 1064 nm, using a short cavity configuration. The Nd:YAG amplifier head is controlled by a high-current laser-diode driver (Cutting Edge Optronics, model PD-2500-CW), which uses a low-noise power supply (Delta Elektronika BV, model SM 35-45). A closed-loop recirculating cooler (Julabo, model FC1200), using distilled water, provides temperature regulation of the amplifier head in a range from ~5°C to 80°C with a stability of ±0.2°C. This temperature control provides a means of setting the centre wavelength of the gain of the Nd:YAG crystal.

As depicted in Fig. 4, the four-mirror resonator (M_1–M_4) of the Nd:YAG ring laser contains two ringdown-cavity mirrors (M_5, M_6; Layertec, concave, ROC = 0.3 m, dia. = 25.4 mm) with high reflectivity (>99.96%) at $\lambda_S \approx 1550$ nm and high transmission (>99%) at $\lambda_P = 1064$ nm. These form a linear ringdown cavity with length $L = L_R$ (~29.5 cm), inside an evacuable gas sample chamber (– – –) which is sealed by an intracavity AR-coated laser window (LW; $T_{\mathrm{opt}} \geq 99.7\%$ at 1064 nm) and a Brewster plate (BP; uncoated fused silica, with 1° wedge angle). The latter transmits p-polarised laser light and forms part of an optical diode [100], together with a $\lambda/2$ waveplate and a Faraday rotator FR (Optics for Research, model IO-5-1064-Z), to ensure uni-directional operation of the ring laser. FR is based on a terbium gallium garnet ($Tb_3Ga_5O_{12}$; TGG) crystal, with 4.8-mm aperture, 10.5-mm length, $T_{\mathrm{opt}} \geq 99.2\%$, and cw damage threshold > 20 kW/cm^2 at 1064 nm; its strong axial magnetic field rotates the plane of polarisation of the intracavity 1064-nm light by ~15° relative to that defined by BP. Our relatively low cw intracavity laser power level avoids complications due to SRS generation [101] and thermally induced birefringence [102, 103] in the TGG crystal. A second $\lambda/2$ waveplate helps to minimise thermally induced birefringence effects in the Nd:YAG laser rod, adapting a well-established approach [104–106].

SLM operation of the Nd:YAG ring laser is achieved by including a solid silica étalon E (Molectron Corp.; FSR, ~1 cm^{-1}; finesse, ~9); the étalon is mounted in an oven, temperature-tuned by an adjustable power supply (ISO-TECH, model IPS2303D). After coarsely setting the laser gain centre wavelength by adjusting Nd:YAG rod temperature (typically in the range 17–19°C), the exact output wavelength of the Nd:YAG ring laser can be finely tuned by adjusting either the tilt angle of the solid étalon or its temperature. The latter (preferred) approach yields a linear tuning rate of ~0.007 nm/°C and allows us to finely tune the Nd:YAG laser wavelength, for instance from ~1064.35 nm to ~1064.45 nm by varying the étalon temperature from 30°C to 45°C.

The spatial mode profile of the intracavity laser beam is controlled by lenses L_1–L_3 (AR-coated at 1064 nm; L_1: plano-concave with $f = -401$ mm; L_2, L_3: plano-convex with $f = 508.3$ mm) to optimise both the performance of the Nd:YAG ring laser and the spatial overlap of the pump and Stokes (probe) beam mode profiles over the entire ringdown-cavity interaction length L_R (~29.5 cm), as summarised in Table 1.

As also depicted in Fig. 4, the cw intracavity laser power of the Nd:YAG ring laser is monitored by measuring the power leakage through cavity mirror M_3, using a power meter (Newport, model 2832-C) with photodetector head (Newport, model 818-IG). Other forms of Nd:YAG laser beam diagnostic that are accessed through cavity mirror M_4 include a wavemeter (Burleigh, model WA-4500; specified accuracy: ±0.02 cm^{-1}) to calibrate wavelength, a laser spectrum analyser (Coherent, model 250; 1.5-GHz FSR) to monitor the spectral mode distribution of the Nd:YAG laser radiation, and a laser beam analyser (Spiricon, model LBA-100A) with a silicon CCD camera (Pulnix, model TM-745) to measure the spatial beam profile. To avoid saturation and optical damage, the monitored laser beam is attenuated by a series of surface reflections off uncoated silica wedges W, to avoid degradation of the beam profile by multi-reflection interference. Wavemeter étalon interference fringes are used to verify SLM operation of the Nd:YAG ring laser. This performance is confirmed by the 1.5-GHz-FSR spectrum analyser

Table 1 Simulated e^{-2} diameters (mm) at three positions inside the ringdown cavity for the Nd:YAG laser pump and Stokes (probe) beams in two different cw SRG-CRD spectrometers, as considered in Sects. 2–4. The beam profiles are adjusted for efficient beam overlap, high Raman gain, and optimal pump-laser operation. The simulations [6] use standard ABCD Gaussian matrix analysis (to treat discrete optical elements such as lenses and mirrors) and finite-element analysis (to model distributed thermal lensing effects in the Nd:YAG rod)

Beam locations (e.g. as illustrated in Fig. 1)	Simulated e^{-2} beam diameters (mm) at three points inside the intracavity ringdown cavity		
	M_5	Mid-point	M_6
Nd:YAG laser pump beam (Sect. 2)	0.75	0.73	0.82
Bi-directional Stokes (probe) beam (Sect. 3)	0.76	0.54	0.76
Uni-directional Stokes (probe) beam (Sect. 4)	0.77	0.49	0.77

which yields a SLM spacing of ~213 MHz (corresponding to a round-trip length of ~1.41 m for the laser ring cavity).

2.2 Simulation and optimisation of pump beam profile

Design of the Nd:YAG ring laser has relied on realistic simulation of the fundamental spatial mode profile of the laser beam inside the ring resonator [6], using standard ABCD Gaussian matrix analysis (e.g. to treat the effect of intracavity lenses L_1–L_3) together with a finite-element analysis procedure to account for thermal lensing effects in the Nd:YAG rod. As an example of many such simulations, we consider a typical diode pump power of ~104 W (corresponding to a diode drive current of ~18 A), which is expected by the manufacturer to produce a positive thermal lens of ~600 mm. As shown in Table 1, the simulated fundamental spatial mode profile of the laser beam inside the ring resonator of the SRG-pump laser is then predicted to yield a minimum e^{-2} diameter of ~0.73 mm in the ringdown cavity formed by mirrors M_5 and M_6; this beam waist is actually offset by ~5 cm from the mid-point of the 29.5-cm ringdown cavity. The e^{-2} diameters of the fundamental spatial mode profile of the intracavity laser beam at the ringdown cavity mirrors depicted in Fig. 4 are ~0.75 mm and ~0.82 mm for M_5 and M_6, respectively. The simulations yield similar results in both the tangential (horizontal) and sagittal (vertical) planes, with calculated e^{-2} beam diameters that differ by less than 0.5%, corresponding to a virtually circular beam profile.

The intracavity power and spectral performance of the cw ring laser depend critically on the actual optical beam path through its Nd:YAG rod. To achieve stable SLM operation while maximising intracavity laser power, the optical beam path through the rod is aligned in a tilted fashion. The spatial mode profile of the laser beam is clipped slightly on the side of one flat end face of the Nd:YAG laser rod; this typically entails a small (~2 W, i.e. ~5% of maximum) trade-off in intracavity laser power. As a result, higher-order transverse modes are better suppressed and lowest-order transverse-mode and SLM operation is achieved. Such alignment is sensitive to small changes, which determine the amount of clipping. It is therefore helpful to precisely maintain the optical beam path through the Nd:YAG laser rod, using aligned irises in the optical beam path of the ring laser as depicted in Fig. 4. These adjustments are guided by diagnostic devices such as the power meter, wavemeter and spectrum analyser.

Under these conditions [6], the laser threshold occurs at a diode drive current of 14.8 A. Above that threshold, the intracavity laser power increases steadily with increasing diode drive current (i.e. increasing diode pump power), with a slope of ~11 W A^{-1}, attaining a maximum of ~27.0 W with a diode drive current of 17.2 A. At this maximum intracavity laser power, the ring laser operates stably in a single longitudinal mode. The intracavity laser power stability is high, with typical fluctuation and drift less than ±0.3% measured over 2-hour periods.

Extensive simulations [6] of the fundamental spatial mode profile of the laser beam inside the ring resonator, performed for a variety of diode pump powers, indicate that the e^{-2} beam diameter of the spatial mode profile inside the ringdown cavity decreases as diode pump power increases. At the same time, however, the spatial mode diameter inside the laser rod increases until it starts to clip the edges of the Nd:YAG rod, when the laser cannot support pure TEM_{00}-mode operation. The laser beam analyser and CCD camera have been used to measure the spatial beam profile of radiation leaking out of the Nd:YAG ring laser cavity through mirror M_4. With an optimal diode pump current of ~17.2 A (which yields stable SLM operation with maximum intracavity laser power). Gaussian least-square fits in the horizontal and vertical directions show that the resulting e^{-2} beam diameters are in the ratio of 0.89 : 1.00 and values of the corresponding times-diffraction-limit parameter M^2 are measured to be 1.05 and 1.27 [6]. The emerging laser beam, as sampled at mirror M_4, therefore has a slightly oval spatial-mode profile, which is attributable to the above-mentioned clipping effect in the Nd:YAG rod. By contrast, our simulations did not take the clipping effect into account, but we expect them to give a reasonably reliable estimate of spatial overlap between the mode profiles of SRG-pump and Stokes (probe) beams over the entire interaction length L_R inside the linear ringdown cavity. A preliminary summary of simulated overlapping beam geometries, attainable within the ringdown cavity of our actual cw SRG-CRD instruments, is presented in Table 1.

An optional element in the Nd:YAG ring laser (illustrated in Fig. 1, but not in Fig. 4) is an intracavity chopper CH that can be used for data-acquisition purposes with background subtraction as further discussed in Sect. 3 below. The intracavity chopper typically operates at a frequency of ∼40 Hz; this enables quasi-cw, steady-state operation of the ring laser, in which the thermal response of the Nd:YAG rod is virtually constant during a chopper cycle.

3 Bi-directional SRG-CRD detection: methodology and results

In this section, we consider in detail two forms of bi-directional cw SRG-CRD spectrometer, using an intracavity linear ringdown cavity; these yield Doppler-limited spectra, as explained in Sect. 1 above, and demonstrated in the following Sects. 3.1 and 3.2.

3.1 SRG-CRD spectroscopy with a single linear ringdown cavity

3.1.1 Design and construction

Here we present details of a Doppler-limited bi-directional cw SRG-CRD spectrometer that has previously been presented briefly in a preliminary paper [5]. Figure 5 comprises a highly detailed schematic of this instrument, incorporating the four-mirror cavity (M_1–M_4) of the Nd:YAG ring laser and its intracavity linear ringdown cavity (M_5–M_6), as already described in Sect. 2.1, in the context of Fig. 4.

The evacuable gas-sample chamber (represented by the – – – rectangle in Figs. 4 and 5) is flexibly designed for the various cw SRG-CRD spectroscopic configurations described in this paper. It comprises a vacuum-welded, electropolished stainless steel box (70 cm long ×14 cm wide ×13.5 cm high; ∼16-L internal volume, including vacuum pump and connector spaces) with a removable lid plate and Viton O-ring vacuum seals on all flanges and windows. The chamber was vacuum-tested down to $\sim 10^{-9}$ Torr. Vacuum ports using ISO-K flanges are located at different points on the chamber walls for optical beam coupling, gas inlets and outlets, pressure gauges and electrical feedthroughs. The gas-handling and vacuum-control system includes inlet and outlet needle valves for gas-sample flow control, a pressure gauge (MKS Baratron, model 122A; pressure range, 0–1000 Torr), a rotary vacuum pump (Alcatel, model 2010), and a liquid-nitrogen trap (MDC, model 434008). A turbomolecular pump (Alcatel, model ATP80) is attached via a large ISO-K flange vacuum port to the lid of the gas-sample chamber, for optional use as a further vacuum pump stage. Optical mounts and other components located inside the gas-sample chamber needed to be vacuum compatible and thoroughly cleaned, in order to minimise out-gassing and possible contamination of the highly reflective CRD mirrors.

The linear ringdown cavity (specified in Sect. 2), as in Figs. 4 and 5, has mirrors M_5 and M_6 separated by $L = L_R = 29.5$ cm, yielding a 505-MHz FSR. The high reflectivity (>99.96%) of these mirrors at $\lambda_S \approx 1550$ nm corresponds to a finesse of at least 7800 and an empty-cavity ringdown time τ_0 of ∼2.5 µs. Simulated geometries of overlapping pump and Stokes beams, actually attainable within this ringdown cavity, have been presented in Table 1 above. Mirrors M_5 and M_6 are attached to compact, mechanically stabilised stainless steel optical mounts, with M_6 mounted on a cylindrical low-voltage PZT element (Piezotechnik, model HPSt-150/20-15/25 VS35), driven by a sinusoidal voltage with peak-to-peak amplitude of ∼11.5 V. This allows rapid modulation of the resonance frequency of the ringdown cavity over a range of ∼1.25 GHz (∼2.5 times its FSR).

The Stokes (probe) laser L_S used here is an external-cavity tunable diode laser (New Focus, model 6262 with controller model 6200). It produces a maximum output power of ∼5 mW in SLM operation and its output wavelength λ_S is continuously picomotor-tunable without mode hops over the communications-band wavelength range 1.5–1.6 µm, with a short-term (∼5 s) optical bandwidth $\Delta\nu_L < 5$ MHz; it also has a PZT-controlled fine-tuning frequency range of ∼60 GHz ($\sim 2\ \mathrm{cm}^{-1}$). Figure 5 shows that this laser L_S is well protected by two Faraday-rotator optical isolators OI_1 and OI_2 (each providing 36-dB isolation at ∼1550 nm). After traversing OI_1 (Optics for Research, model IO-4-1550-HP) and a half-wave plate ($\lambda/2$) for polarisation adjustment, the free-space output radiation from laser L_S is coupled via an aspherical collimating lens L_4 (Thorlabs, model F220FC-155) into a single-mode optical fibre (Thorlabs, model P3-6324-FC-5) which also serves as a spatial filter, and an additional fibre-optical isolator (FOI).

The radiation emerging from the single-mode fibre is collimated by another aspherical collimating lens L_5 (Newport, model F-LA11). The SLM Stokes (probe) beam passes through OI_2 (Optics for Research, model IO-4-IR2-HP) with a power of ∼1 mW at $\lambda_S \approx 1550$ nm. It is directed to the rapidly-swept ringdown cavity via flat high reflectors M and a lens L_6 ($f = 0.4$ m) that is used to mode-match it to the fundamental TEM_{00} mode of the ringdown cavity; fine adjustment of L_6 is able to reduce residual transverse mode intensities to <1% of the fundamental-mode signal intensity. To minimise reflection losses, the probe beam enters and exits the gas-sample chamber through Brewster-angle windows (uncoated fused silica, with 1° wedge angle). (Incidentally, optical elements in the beam such as fibre input facets, lenses, filters and waveplates are slightly tilted with respect to the propagation axis, to avoid interferences from back reflections and étalon effects. Likewise,

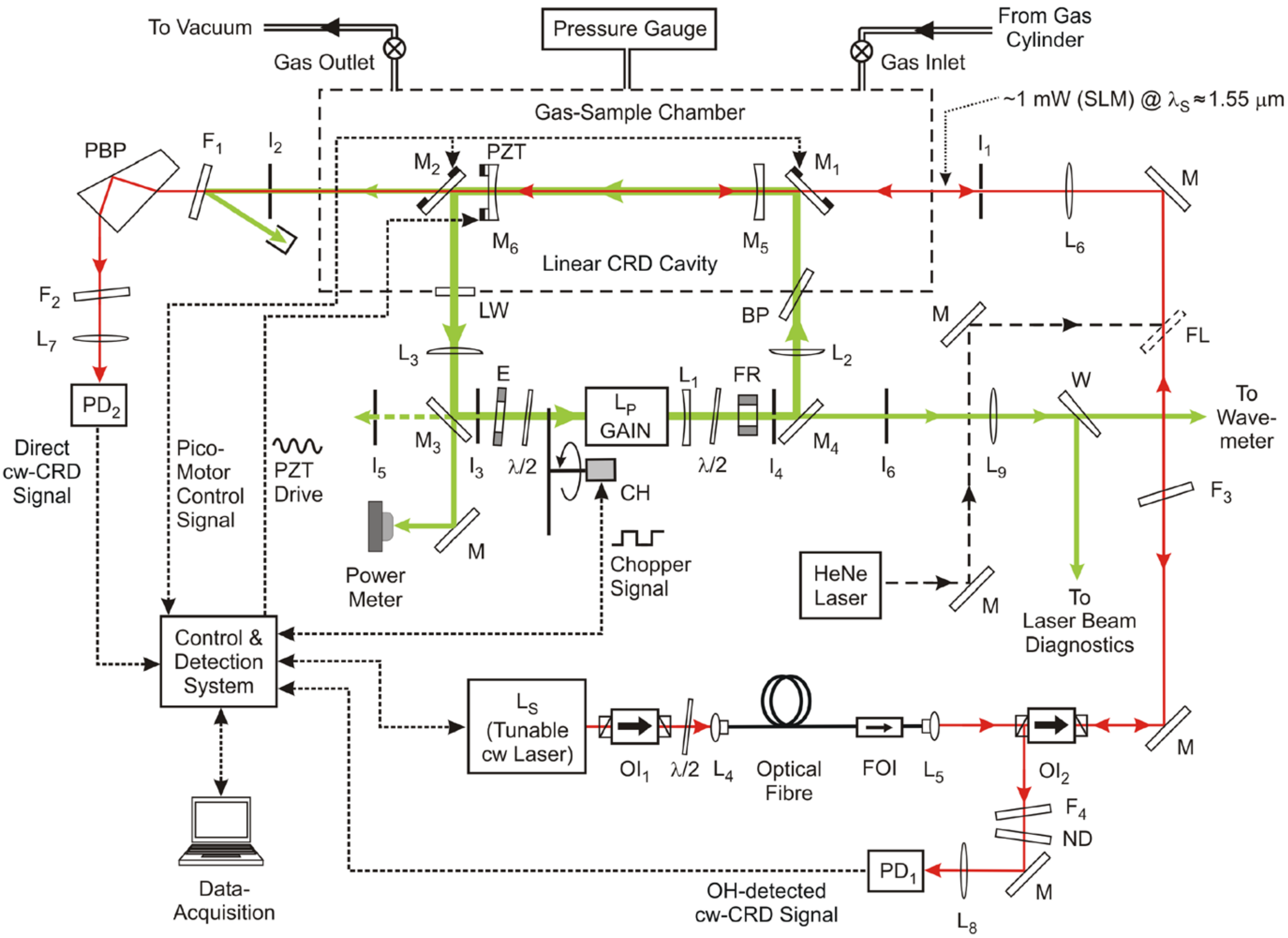

Fig. 5 Detailed layout of a cw SRG-CRD spectrometer based on a linear ringdown cavity (M_5–M_6, inside an evacuable gas-sample chamber) within the four-mirror cavity (M_1–M_4) of a Nd:YAG ring laser. This is as in Fig. 4, with addition of a mechanical chopper CH, a photodetectors PD_1 and PD_2 (for backward- and forward-propagating CRD detection, respectively), assorted optical elements, and connections for electronic (– – –) and gas (===) control. As in Fig. 1, coherent cw beams from the Nd:YAG pump laser (uni-directional *broad arrowed line*) and the Stokes probe laser L_S (bi-directional *fine arrowed line*) are co-focused and aligned to optimise their coherent Raman interaction. See text for further details

ringdown-cavity mirrors M_5 and M_6 are slightly wedged and/or used off-centre. Polarisation-maintaining fibres are not used in any of our cw CRD detection schemes, in order to avoid an elliptical Stokes (probe) beam profile, which would degrade the mode matching in the ringdown cavity.)

After passing through (and interacting with) the linear ringdown cavity inside the gas-sample chamber, the Stokes (probe) beam at λ_S is processed by filters F_1 and F_2, each a high reflector at 1064 nm (CVI, model Y1-1037-0, flat) but with ~97% transmission at $\lambda_S \approx 1550$ nm, and a Pellin Broca prism (PBP) that rejects very small residual amounts of pump radiation passing through filter F_1. These measures ensure that only 1550-nm Stokes (probe) radiation reaches photodetector PD_2 via a focusing lens L_7 ($f = 50$ mm), averting power saturation damage from small amounts of pump radiation. A pair of irises I_1 and I_2 is used to define the alignment of the Stokes (probe) beam, with the ringdown time actively monitored during the CRD optimisation procedure. A HeNe laser tracer beam may also be coupled into the system via a flipper mirror FL, to facilitate optical beam path checks during alignment.

The alternative OH (optical heterodyne) mode of cw CRD detection is also depicted in Fig. 5, where backward-propagating Stokes (probe) light at ~1550 nm is reflected actively from the ringdown cavity [26–28]. The Faraday-rotator optical isolator OI_2 includes a polarising beamsplitter that diverts the backward-propagating OH-detected light via a focusing lens L_8 ($f = 75$ mm) onto the photodetector PD_1. This light passes through filters F_3 and F_4 (identical to F_1 and F_2) and a suitable neutral density filter ND, thereby rejecting unwanted 1064-nm SRG-pump radiation.

Each of the photodetectors PD_1 (New Focus, model 1811-FS; 125-MHz bandwidth) and PD_2 (New Focus, model 2053-FS; 10-MHz bandwidth) comprises a InGaAs/

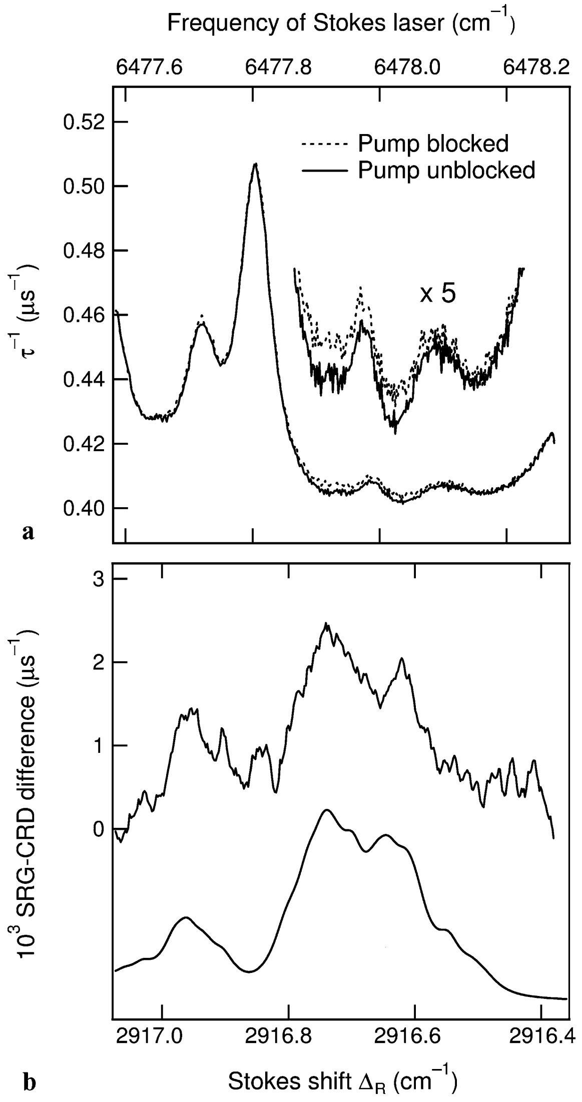

Fig. 6 Panel (**a**) shows CRD spectra of $^{12}CH_4$ gas ($p = 250$ Torr, $T = 296$ K), recorded by scanning the wavelength λ_S of a cw tunable probe laser in the vicinity of ~1544 nm; the upper pair of traces is a vertically offset, fivefold expansion of the lower pair of traces. The *solid traces* in panel (**a**) are recorded with SRG-pump laser wavelength $\lambda_P = 1064.42$ nm and peak irradiance $I_P^{(0)} = 16$ kW cm^{-2} (at the beam waist in the centre of the linear ringdown cavity as in Fig. 5) and include a minor SRG-CRD contribution due the 2916.5-cm^{-1} ν_1 Raman band of $^{12}CH_4$. This is distinguished from the major CRD absorption background (*dashed traces*) that is recorded while the pump-laser cavity is blocked by means of a 40-Hz mechanical chopper. Note that, unusually, τ^{-1} decreases (i.e. τ increases) as λ_S is tuned through the peak of the SRG spectrum. Panel (**b**) compares the resulting observed bi-directional cw SRG-CRD difference spectrum (*upper trace*, after digital smoothing) to a Voigt-profile model spectrum (*lower trace*, vertically offset) based on preferred spectroscopic [66, 67] and relative SRG intensity [81] data, as outlined in Sect. 1.3, with the difference frequency ($\omega_P - \omega_S$) scanned through successive Raman transition frequencies Δ_R [5]

PIN photodiode with matching low-noise preamplifier for a wavelength range of 0.9–1.7 µm; these are used to detect backward- and forward-propagating swept-cavity cw CRD signals, respectively [25–28]. The minimum noise-equivalent power (NEP) specified for PD_1 (NEP = 2.5 pW Hz$^{-1/2}$) is ~7.5 times less sensitive than that of PD_2 (NEP = 0.34 pW Hz$^{-1/2}$). A low-pass filter (with its time constant much smaller than the ringdown time constant τ) is used to smooth the oscillatory part of the CRD signal decay waveform registered by PD_2. While PD_2 provides higher sensitivity and lower noise for directly transmitted (forward-propagating) cw CRD signal detection, its 10-MHz bandwidth makes the same form of photodetector unsuitable for detection of the rapidly oscillating OH-detected cw CRD signals that are monitored in the backward-propagating direction by PD_1, which has higher bandwidth but is less sensitive.

To overlap the SRG-pump beam with the aligned Stokes (probe) beam over the entire interaction length L_R of the ringdown cavity while maintaining optimum pump-laser performance, it is necessary to adjust the pump-laser cavity mirrors M_1–M_4 after the gas-sample chamber has been closed. Mirrors M_1 and M_2, which are located inside the gas-sample chamber, are therefore held in precision motorised multi-axis optical mounts (New Focus, model 8809-C with model 8801 picomotors and model 8620 control pad) for remote alignment. The challenging iterative alignment procedure is facilitated by means of aligned irises I_3–I_6 in the optical beam path of the pump laser. A tiny portion of the pump radiation that leaks through M_4 is conveyed by lens L_9 ($f = 750$ mm) and wedge W into a wavemeter and other beam diagnostic devices, as already outlined in Sect. 2.

The CRD signals from photodetectors PD_1 and PD_2 are recorded by a high-performance dual-channel digitiser (National Instruments, model NI PCI-5122, with 100-MS s^{-1} real-time sampling, 100-MHz bandwidth, 14-bit vertical resolution, and 32-MB onboard acquisition memory per channel). Software written in LabVIEW format has been developed to process the CRD signals and to scan the wavelength λ_S of the tunable Stokes (probe) laser.

At a given Stokes (probe) laser wavelength λ_S, the SRG-CRD detection cycle entails measuring sets (typically six) of PZT-driven cavity sweeps with the intracavity chopper aperture closed (i.e. the 1064-nm pump-laser cavity is blocked) and using a synchronised electronic gate to log the direct and OH-detected CRD waveforms from one of those sweeps (typically the fourth). A number (n) of background ("without pump") CRD waveforms are averaged and a ringdown rate τ_B^{-1} extracted by an appropriate fitting procedure [6, 28] and a further number (m) of similar sets of τ_B^{-1} values yield a grand average $\langle\tau_B^{-1}\rangle$ of ($n \times m$) background ringdown rate measurements. This process is then repeated with intracavity chopper aperture open (i.e. the 1064-nm pump-laser cavity is unblocked) and an identical number

$(n \times m)$ of SRG-pumped ringdown rate measurements yields another grand average $\langle\tau_{\mathrm{P}}^{-1}\rangle$ ("with pump"). CRD spectra with and without SRG pumping are then obtained by plotting $\langle\tau_{\mathrm{P}}^{-1}\rangle$ and $\langle\tau_{\mathrm{B}}^{-1}\rangle$, respectively, against λ_{S} or ω_{S}. Similarly, a cw SRG-CRD difference spectrum is obtained by plotting $(\langle\tau_{\mathrm{P}}^{-1}\rangle - \langle\tau_{\mathrm{B}}^{-1}\rangle)$ against λ_{S} and hence (given the pump wavelength λ_{P}) the Stokes shift $\Delta_{\mathrm{R}} = (\omega_{\mathrm{P}} - \omega_{\mathrm{S}})$.

3.1.2 Performance and spectroscopic results

Figure 6 presents results derived by this process, in the context of the ν_1 fundamental rovibrational Raman band of $^{12}\mathrm{CH}_4$ gas, using the 10-MHz low-noise photodetector PD$_2$ for directly transmitted (forward-propagating) cw CRD measurements. Each data point, in the pairs of spectra of Fig. 6(a), is the average of $(n \times m) = 256$ rapidly-swept CRD signal waveforms, typically with m $(= 32)$ groups of n $(= 8)$ waveforms apiece. Each of the m groups of averaged directly transmitted cw CRD signal waveform is processed by a Levenberg–Marquardt algorithm [107–109] to fit an exponentially decaying model function with ringdown rate τ_{B}^{-1} or τ_{P}^{-1} for without- or with-pump situations, respectively. A data-rejection procedure is applied, with up to ~5% of the τ_{B}^{-1} or τ_{P}^{-1} values eliminated on the basis that they differ from the corresponding mean $(\langle\tau_{\mathrm{B}}^{-1}\rangle$ or $\langle\tau_{\mathrm{P}}^{-1}\rangle)$ by more than 2 standard deviations. To record the spectra depicted in Fig. 6(a), the wavelength λ_{S} of the Stokes (probe) laser is incremented with a step size of $\sim 5.5 \times 10^{-4}$ nm ($\sim 2.3 \times 10^{-3}$ cm^{-1} or ~70 MHz); they comprise ~340 pairs of data points recorded during a period of ~50 min.

From the noise level in the CRD spectra in Fig. 6(a), we deduce that MDLG $= 1.6 \times 10^{-8}$ cm^{-1}; recognising that the time interval taken to measure each data point in Fig. 6(a) is $t_{\mathrm{M}} = 9$ s, we obtain MDLG$_N = 5 \times 10^{-8}$ cm^{-1} Hz$^{-1/2}$. This sensitivity corresponds to our preliminary report in the context of cw SRG-CRD spectroscopy [5], as discussed in Sect. 1.3 above. This performance is superior by a factor of almost 3 to our earlier cw SRG-CRD measurements (prior to implementation of the 10-MHz low-noise photodetector PD$_2$, dual-channel high-performance digitiser, and associated data-processing refinements) [5, 6]. A key design element in our data-processing and analysis procedures is to reduce dead times and increase the overall execution speed (and hence minimise the MDLG normalisation factor $N^{-1/2}$). With both SRG-pumped and background CRD signal waveforms acquired in real time at high speed, main factors that influence the overall execution speed are twofold:

- The chopper frequency (typically 40 Hz), which determines the data rate at which the CRD signal waveforms can be acquired; this is limited by the need to ensure good operating conditions of the SRG-pump laser, such as the stability of its optical frequency and SLM quality.
- The time taken to fit CRD signal waveforms to an appropriate model function (as outlined above) and thereby determine their ringdown times τ; this is optimised by means of the above-mentioned data-processing procedures for $(n \times m) = 256$ rapidly-swept CRD signals, with m $(= 32)$ groups of n $(= 8)$ averaged waveforms apiece.

It is evident (as inferred in Sect. 1.3 and previously reported [5]) that the $\langle\tau_{\mathrm{B}}^{-1}\rangle$ (– – – –, without pump, background) and $\langle\tau_{\mathrm{P}}^{-1}\rangle$ (———, with pump, SRG-pumped) traces in Fig. 6(a) differ by very little, despite our strenuous efforts to maximise the SRG-CRD contribution. As shown in the lower trace of Fig. 3, the most prominent linear absorption peak in the spectra of Fig. 6(a), at ~6477.8 cm^{-1} (~1543.7 nm), is the only one assigned in the HITRAN 2004 spectroscopic database [86]. The observed cw SRG-CRD spectrum for the ν_1 fundamental rovibrational Raman band of $^{12}\mathrm{CH}_4$ gas is shown in the upper trace of Fig. 6(b) [5]. It comprises the difference $(\langle\tau_{\mathrm{P}}^{-1}\rangle - \langle\tau_{\mathrm{B}}^{-1}\rangle)$ between the two traces in Fig. 6(a), after digital smoothing by a Savitzky–Golay 19-point, 4th-order moving-window polynomial procedure [110–112] and ~30-fold magnification of its ordinate scale relative to that of Fig. 6(a).

The lower, offset trace of Fig. 6(b) is a simulated SRG spectrum [5], generated by a Voigt-profile model based on preferred spectroscopic [66, 67] and relative SRG intensity [81] data, as explained in the final five paragraphs of Sect. 1.3 above. The observed (upper) and simulated (lower) SRG spectral band contours shown in Fig. 6(b) are generally in satisfactory agreement, apart from the deeper dip at ~2916.7 cm^{-1} in the former. This discrepancy may be attributed to possible ongoing inadequacies in the model CARS and SRS spectra of $^{12}\mathrm{CH}_4$ (as discussed in Sect. 1.3). The experimental cw SRG-CRD spectrum has been recorded with the SRG pump-laser wavelength $\lambda_{\mathrm{P}} = 1064.42$ nm, which allows the main Q-branch peak in the ν_1 fundamental rovibrational Raman band of $^{12}\mathrm{CH}_4$ gas, with Stokes shifts $\Delta_{\mathrm{R}} = 2916.4$–$2916.8$ cm^{-1}, to be situated within a gap in the background linear absorption spectrum, as the difference frequency $(\omega_{\mathrm{P}} - \omega_{\mathrm{S}})$ is tuned through successive Raman transition frequencies Δ_{R}. However, regions of the SRG spectrum at Stokes shifts Δ_{R} above 2916.8 cm^{-1} are then subject to higher background-subtraction noise, which may give rise to apparently spurious features in the experimental cw SRG-CRD spectrum. For instance, such features observed in Fig. 6(b) at ~2916.90 cm^{-1} and ~2916.85 cm^{-1} are overlapped by the strong peaks at ~6477.8 cm^{-1} and ~6477.7 cm^{-1} in the background spectrum of Fig. 6(a); similar apparently spurious features recur in other experimental cw SRG-CRD spectra that are reported in Sects. 3.2 and 4.

The background-subtraction noise was characterised during performance tests of the cw SRG-CRD spectrometer with the gas-sample chamber containing $^{12}\mathrm{CH}_4$ gas $(p =$

100 Torr, $T = 296$ K) [6]; subtraction of two supposedly identical background spectra failed to give a perfect null when the Stokes (probe) laser wavelength λ_S was tuned through any of the prominent peaks (e.g. those with ω_S ~6477.8 cm^{-1} and ~6477.7 cm^{-1}, as noted above) in the absorption spectrum of $^{12}CH_4$. This effect is attributed to tiny drifts and scan nonlinearities of Stokes (probe) laser frequency during the spectroscopic scan; it gives rise to residual features in the difference spectrum that match the shape of the derivative of the CRD absorption spectrum. To minimise this effect, it was found helpful to reset the Stokes (probe) wavelength λ_S to its starting value before incrementing it to the next point in a spectroscopic scan. The "dead time" of ~1.0 s per increment required for the laser frequency to settle is efficiently used for program tasks such as waveform extraction from the digitiser, switching of synchronised gate position, and fitting of CRD signal waveforms. Although the problem of background-subtraction noise is largely remedied by this approach, spurious minor features persist, as noted in the context of the upper trace of Fig. 6(b).

In view of the relatively low irradiances employed in all of our cw SRG-CRD experiments, we can dismiss the possibility that our SRG spectra, such as that observed in Fig. 6(b), might be affected by the AC Stark effect. For instance, this effect has been found [113, 114] to occur in CARS spectroscopy when higher optical irradiances are used. Indeed, AC Stark effects have been reported [4, 73] in the context of the ν_1 Raman band of $^{12}CH_4$ gas. However, the maximum pump-beam irradiance used in our experiments $I_P^{(0)} = 16$ kW cm^{-2} (at the beam waist in the centre of the linear ringdown cavity as in Fig. 5) is ~10^6 less than those employed ($\geq$10 GW cm^{-2}) in previous quasi-cw coherent Raman experiments [4, 73].

3.1.3 *Mechanistic implications*

As previously reported in preliminary fashion [5], Fig. 6 demonstrates that a cw SRG-CRD difference spectrum for the ν_1 fundamental rovibrational Raman band of $^{12}CH_4$ gas can be measured (not without difficulty) in the presence of a dominant background contribution from linear absorption in weak overtone bands of $^{12}CH_4$ that overlap and tend to mask the even weaker SRG-CRD spectrum of interest. Efficient extraction of the very small Raman signal with acceptable spectroscopic precision, detection sensitivity, and signal-to-noise ratio (SNR) requires background-subtraction measures that are far from trivial. As previously reported [5], the SRG-CRD contribution can be distinguished from the background CRD absorption spectrum because the former shifts on the scale of the Stokes wavelength λ_S if the SRG-pump laser wavelength λ_P is varied (by altering the temperature of the Nd:YAG gain medium L_P) while the latter is fixed on the λ_S scale. As demonstrated in Fig. 2 of [5], features in the SRG-CRD spectrum occur consistently at well-defined values of the Stokes shift Δ_R. We have also demonstrated in Fig. 3 of [5] that ν_1-band contours of rovibrational cw SRG-CRD spectra over a range of $^{12}CH_4$ pressures ($p = 250$–760 Torr) are consistent with those from optically detected SRG spectroscopic measurements [20].

A significant phenomenological outcome of Fig. 6 is that CRD signals corresponding to background absorption appear as an *increase* in τ^{-1} (i.e. the usual loss-induced decrease in ringdown time τ), independent of whether pump radiation from the pump laser is blocked by the chopper or not, whereas the SRG-CRD signals appear as a *decrease* in τ^{-1} (i.e. an unusual increase in τ, as discussed in the final three paragraphs of Sect. 1.2) if the SRG-pump laser cavity is not blocked by the chopper. This phenomenon identifies genuine SRG signals and helps us to measure them against the predominant linear absorption background.

As discussed previously [5] and in Sect. 1.3 above, the band contour of the cw SRG-CRD spectrum in Fig. 6(b) arises from a 1:1 superposition of co- and counter-propagating SRG-pump and Stokes (probe) beams with small and large Doppler linewidth contributions respectively. The bi-directional configuration used in the intracavity-pumped cw SRG-CRD system of Fig. 5 therefore fails to optimise spectroscopic resolution. A narrower-band uni-directional cw SRG-CRD instrument, with co-propagating SRG-pump and Stokes (probe) beams has been introduced in Fig. 1 and will be discussed in further detail in Sect. 4 below.

3.2 SRG-CRD spectroscopy with two linear ringdown cavities

3.2.1 *Design and construction*

To enhance the data rate attainable with the bi-directional cw SRG-CRD spectrometer described in Sect. 3.1, we have assembled a more advanced instrument with a second, zero-I_P linear ringdown cavity as a reference channel. This enables CRD absorption spectra with and without SRG-pumping to be acquired simultaneously, rather than sequentially with the pump laser successively blocked and unblocked as in Sect. 3.1.

Our dual-ringdown-cavity approach to cw SRG-CRD spectroscopy, as illustrated in Fig. 7, facilitates chopper-free subtraction of troublesome infrared-absorption background signals in real time. It also offers the possibility of a cw SRG-CRD spectrometer with higher detection sensitivity, increased duty factor and data rate, and improved frequency- and SLM-stability of the SRG-pump laser (L_P).

As shown in the upper half of Fig. 7, SRG-pumped CRD spectra are still acquired by using the intracavity-pumped cw SRG-CRD spectrometer system as described in the context of Fig. 5, but without needing to use an intracavity

Fig. 7 Layout of a cw SRG-CRD spectrometer with a linear ringdown cavity (M_5–M_6, inside the upper gas-sample chamber) as in Fig. 5 and a zero-I_P ringdown cavity (M_7–M_8, inside the lower gas-sample chamber) added for reference purposes. No chopper is used in this cw SRG-CRD instrument, which enhances the data-acquisition rate. See text for further details

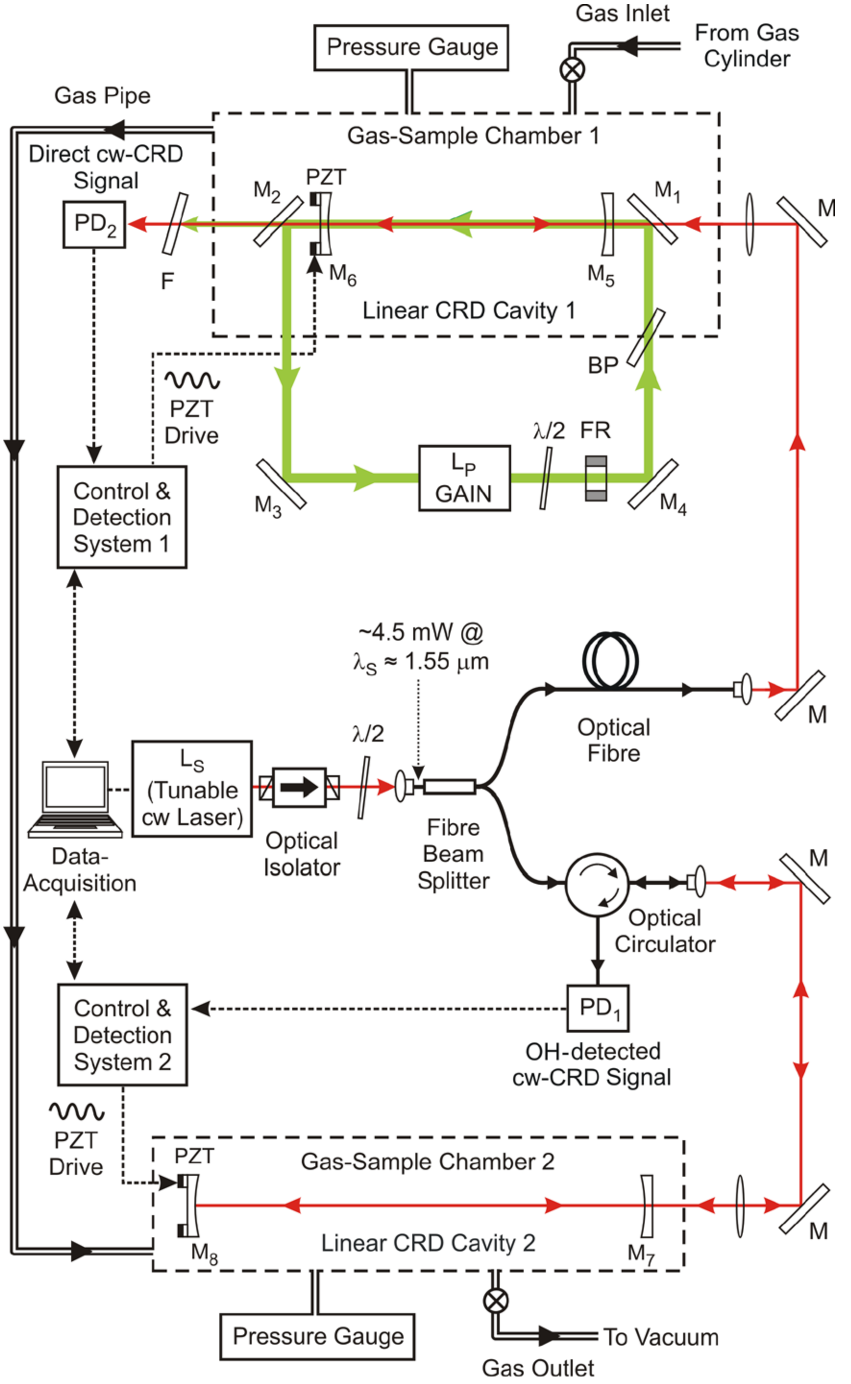

chopper. The lower portion of Fig. 7 shows a second, zero-I_P ringdown cavity (cavity 2) that is used to record background CRD absorption spectra without accessing the SRG-pump laser. Compared to the mirrors (M_5 and M_6, as in Sect. 3.1) of SRG-pumped ringdown cavity 1, the mirrors (M_7 and M_8) in the zero-I_P ringdown cavity 2 do not need to be highly transmissive at the pump wavelength λ_P and can therefore be optimised solely at the Stokes (probe) wavelength λ_S (∼1550 nm) for much higher reflectivity than in ringdown cavity 1. This results in longer ringdown time constants τ and allows background CRD absorption spectrum to be recorded with increased SNR.

Many components of the instrument portrayed in Fig. 7 are common to those of Fig. 5 and some (e.g. details of the ring pump laser, beam-alignment irises and HeNe laser, filters and focusing optics for PD_1 and PD_2, power meter, wavemeter and other laser beam diagnostics) are not depicted in the interests of simplicity. Stokes (probe) laser radiation (frequency ω_S) from a single cw tunable diode laser L_S (New Focus, model 6262 with controller model 6200) is transmitted to cavities 1 and 2 during a spectroscopic scan, thereby ensuring that identical frequency scales apply to cw CRD absorption spectra simultaneously recorded with and without SRG-pumping. This is achieved by splitting the output power of $\mathrm{L_S}$ into two equal parts using a 50:50 fibre beam splitter. By using single-mode fibres designed for the wavelength region of ∼1.5 µm (Thorlabs, model P3-SMF28-FC-5), output powers of ∼2.1 mW at λ_S can therefore be launched simultaneously into the intracavity-pumped cw SRG-CRD spectroscopic system (cavity 1) and the zero-I_P reference system (cavity 2). The two swept-cavity CRD systems have interconnected gas-sample chambers to maintain a uniform gas pressure, as depicted in Fig. 7.

The intracavity SRG-pumped cw SRG-CRD spectrometer (portrayed in the upper half of Fig. 7) based on the linear ringdown cavity 1 is operated as described in detail in Sect. 3.1, with refinements such as the 10-MHz low-noise photodetector (for directly transmitted forward-propagating swept-cavity CRD detection) and the high-performance digitiser, but without the intracavity chopper. Out-gassing from the vacuum-customised motorised mirror mounts (New Focus, model 8809-C) was experienced for gas-sample pressures p less than ∼250 Torr and this was found to impair the high reflectivity of the CRD mirrors ($\mathrm{M_5}$, $\mathrm{M_6}$) to a level where the empty-cavity ringdown time τ_0 declined to ∼1.1 µs. This out-gassing problem was overcome by wrapping each motorised optical mount in a layer of aluminium foil. The high reflectivity of the CRD mirrors ($\mathrm{M_5}$, $\mathrm{M_6}$) was thereby recovered and the empty-cavity ringdown time τ_0 was increased to ∼5.5 µs by careful alignment to access parts of the mirror surface with notably high reflectivity R (∼99.98%). This comprises a twofold improvement on the Layertec-specified value of $(1 - R)$ for such mirrors and a corresponding improvement in CRD sensitivity, relative to that in Sect. 3.1 and elsewhere [5].

The swept-cavity cw CRD reference spectrometer with its zero-I_P linear ringdown cavity 2 is portrayed in the lower half of Fig. 7; it has been described in detail elsewhere [28], with a remarkably high sensitivity (MDLG $\equiv$ MDAL $\approx 5 \times 10^{-10}$ $\mathrm{cm^{-1}\,Hz^{-1/2}}$) [28]. Its two mirrors ($\mathrm{M_7}$, $\mathrm{M_8}$; Los Gatos Research; 1-m concave radius, 25.4-mm diameter, and 1° wedge angle) do not need to transmit 1064-nm pump radiation and so are obtainable with a much higher reflectivity R (∼99.993% at $\lambda_\mathrm{S} = 1550$ nm) than is possible for the intracavity SRG-pumped ringdown cavity 1. The mirror separation of ringdown cavity 2 is set at $L = L_\mathrm{R} = 53.1$ cm to form a high-finesse optical cavity with non-degenerate mode structure for which successive longitudinal-mode ringdown-decay events are effectively isolated. Its empty-cavity ringdown time τ_0 is ∼25 µs and its FSR is 0.28 GHz (0.0094 $\mathrm{cm^{-1}}$) [28]. As depicted in Fig. 7, the gas-sample chambers 1 and 2 for the two rapidly-swept CRD systems are linked by a permanent vacuum connection, enabling them to be operated in unison *either* as flow cells connected in series (e.g. to minimise outgassing at low pressure) *or* with a static fill.

As explained above, half of the Stokes (probe) radiation at λ_S from laser $\mathrm{L_S}$ is delivered to the zero-I_P ringdown cavity 2 via the fibre beam splitter and a single-mode optical fibre. As shown in Fig. 7, it passes through a three-port fibre-optical circulator (AOC Technologies, model OCIR-3155, with isolation, directivity and return loss >50 dB) and is transmitted to ringdown cavity 2, after collimation and matching to the longitudinal-mode geometry of the cavity 2 by means of two focusing lenses. The three-port circulator serves not only as an additional optical isolator to protect $\mathrm{L_S}$ but also as a means of diverting reflected Stokes (probe) laser radiation and backward-propagating ringdown radiation to photodetector $\mathrm{PD_1}$ (New Focus, model 1811-FS; 125-MHz bandwidth, as in Sect. 3.1 and Fig. 5) for OH-detected CRD measurements [26–28].

Directly transmitted forward-propagating cw CRD signals could be conventionally detected, using another photodetector beyond cavity 2, but we prefer here to measure backward-propagating OH-detected cw CRD signals by means of $\mathrm{PD_1}$. As in previous OH-detected rapidly-swept CRD work [27, 28, 88, 89], we use a demodulating logarithmic amplifier (Analog Devices, model AD8307; bandwidth DC–500 MHz, linearity ±1 dB, dynamic range 92 dB) to convert exponentially decaying full-wave oscillatory envelopes of OH into a functional form to enable straightforward linear fitting of the ringdown time τ.

The procedures developed to acquire, process and analyse experimental cw SRG-CRD spectroscopic data with the intracavity-pumped spectrometer described in Sect. 3.1 and Fig. 5 have been modified to operate without the intracavity chopper in the dual-ringdown-cavity cw SRG-CRD spectrometer configuration. The OH-detected zero-I_P cw CRD signals from $\mathrm{PD_1}$ are logged by one channel of the high-performance dual-channel digitiser (National Instruments, model NI PCI-5122, as in Sect. 3.1). This is synchronised to the data-collection operations of the SRG-pumped CRD spectrometer control and detection system 1, in which the other NI PCI-5122 digitiser channel is implemented.

3.2.2 *Performance and spectroscopic results*

This dual-ringdown-cavity cw SRG-CRD spectrometer configuration's performance has been investigated by measuring a sample of $^{12}\mathrm{CH_4}$ gas ($p = 200$ Torr, $T = 296$ K), with the interconnected gas-sample chambers 1 and 2 statically filled. The pair of traces depicted in the Fig. 8(a) (together with their fivefold-magnified insets) are the simultaneously recorded CRD absorption spectra with and without SRG-pumping, corresponding, respectively, to average ringdown rates $\langle\tau_{\mathrm{P}}^{-1}\rangle$ (———) and $\langle\tau_{\mathrm{B}}^{-1}\rangle$ (– – – –, i.e. the zero-I_{P} background).

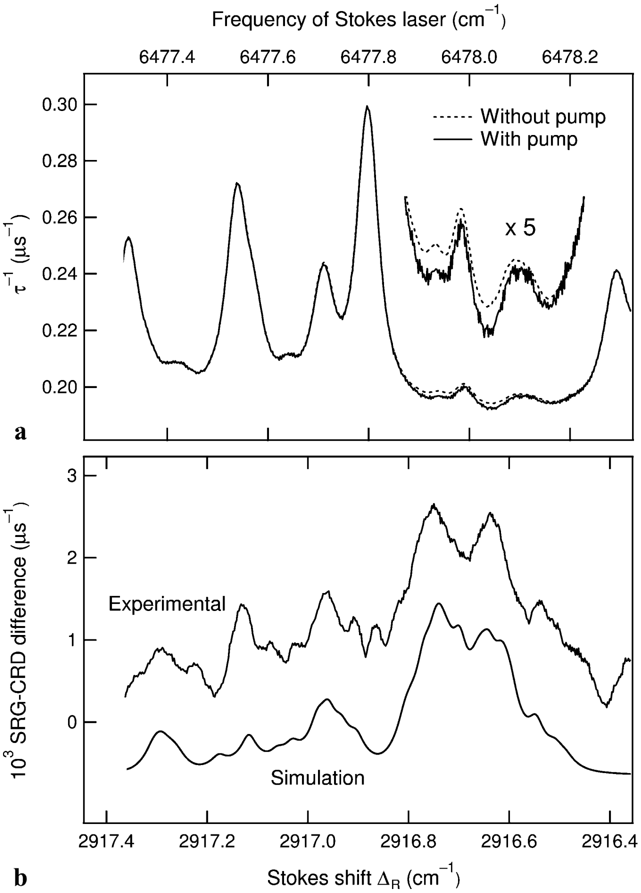

Fig. 8 CRD spectra of ^{12}CH$_4$ gas ($p = 200$ Torr, $T = 296$ K), similar to those in Fig. 6, except that they are recorded with the dual-ringdown-cavity form of cw SRG-CRD spectrometer, as depicted in Fig. 7. The Stokes (probe) light propagates bi-directionally in a linear ringdown cavity. *Solid* and *dashed lines* in panel (**a**) show raw CRD spectra obtained from the two ringdown cavities with and without SRG-pump irradiation, respectively, from which the observed cw SRG-CRD difference spectrum in the upper trace of panel (**b**) is derived. This cw SRG-CRD spectrum for the 2916.5-cm^{-1} ν_1 Raman band of ^{12}CH$_4$ is compared with a simulated SRG-CRD band contour (*lower trace*). See text for further details

As in Sect. 3.1, in Fig. 5, and in our original paper [5], the major contribution to the pair of traces in Fig. 8(a) is the weak absorption spectrum of ^{12}CH$_4$ that is nevertheless very much stronger than the SRG-CRD spectrum of interest. These two spectra need to be subtracted to determine the observed cw SRG-CRD difference spectrum ($\langle\tau_{\mathrm{P}}^{-1}\rangle - \langle\tau_{\mathrm{B}}^{-1}\rangle$), which is plotted in the upper trace of Fig. 8(b) as a function of the Stokes shift $\Delta_{\mathrm{R}} = (\omega_{\mathrm{P}} - \omega_{\mathrm{S}})$ for the ν_1 fundamental rovibrational Raman band of ^{12}CH$_4$ gas.

The experimental cw SRG-CRD spectrum in Fig. 8(b) has been digitally smoothed and its ordinate is magnified by a factor of ~30 relative to that of Fig. 8(a), using procedures as in the context of Fig. 6 in Sect. 3.1. The frequency scales of the recorded CRD spectra in Fig. 8(a) and the resulting cw SRG-CRD difference spectrum in Fig. 8(b) have been linearised and calibrated by using the positions of known ^{12}CH$_4$ absorption features [86, 87], in combination with the corresponding swept-frequency cw CRD absorption spectrum of ^{12}CH$_4$ recorded in Fig. 3. The experimental spectra of Fig. 8 contain ~450 data points, recorded during a period of ~30 min with the same step size as in Fig. 6 but with a data rate that is a factor of ~2.2 higher.

Each data point in the pair of CRD spectra in Fig. 8(a) is a grand average of $(n \times m) = 1024$ ringdown-rate measurements of, where n $(= 32)$ swept-cavity CRD waveforms are averaged and fitted to yield a value of τ_{p}^{-1} or τ_{B}^{-1} and then m $(= 32)$ such fitted τ_{p}^{-1} or τ_{B}^{-1} values are further averaged to yield the overall average values $\langle\tau_{\mathrm{P}}^{-1}\rangle$ (———) or $\langle\tau_{\mathrm{B}}^{-1}\rangle$ (– – – –). As in Sect. 3.1, individual values of τ_{B}^{-1} or τ_{P}^{-1} are rejected if they deviate by more than 2 standard deviations from the corresponding mean ($\langle\tau_{\mathrm{B}}^{-1}\rangle$ or $\langle\tau_{\mathrm{P}}^{-1}\rangle$).

Compared to the performance of the single-ringdown-cavity cw SRG-CRD system as in Sect. 3.1, the dual-ringdown-cavity cw SRG-CRD spectra show superior noise-limited sensitivities (MDLG $= 1.3 \times 10^{-8}$ cm^{-1}; MDLG$_N$ $= 2.6 \times 10^{-8}$ cm^{-1} Hz$^{-1/2}$, normalised to $t_{\mathrm{M}} = 4.1$ s per data point). This MDLG$_N$ value represents a twofold improvement in sensitivity, attributable to higher CRD mirror reflectivities and the faster data rate associated with the dual-ringdown-cavity approach. This yields in turn an improved SNR in the upper trace of Fig. 8(b), with $p = 200$ Torr, compared to its counterpart in Fig. 6(b), with $p = 250$ Torr.

A simulated SRG spectrum [5], generated by our Voigt-profile model and based on preferred spectroscopic [66, 67] and relative SRG intensity [81] data (see Sect. 1.3), is presented in the lower, offset trace of Fig. 8(b). The Doppler linewidths $\Delta\nu_{\mathrm{D}}$ for co- and counter-propagating SRG-pump and Stokes (probe) beams are as in Sects. 1.3 and 3.1, but the FWHM Lorentzian collisional linewidth $\Delta\nu_{\mathrm{C}}$ is reduced by a factor of 0.8 to 0.84 GHz (0.028 cm^{-1}), in view of the lower sample pressure.

As before, the experimental (upper) and simulated (lower) SRG spectral band contours shown in Fig. 8(b) are generally in satisfactory agreement. However, a few apparently spurious features (e.g. at Δ_{R} values of 2916.90 cm^{-1}, 2917.05 cm^{-1}, and 2917.25 cm^{-1}) persist in the experimental cw SRG-CRD spectrum, especially in portions of the background spectrum in Fig. 8(a) where strong linear absorption is likely to aggravate background-subtraction noise and is only partly remedied by resetting λ_{S} to its starting value before incrementing it to the next point in a spectroscopic scan.

4 Uni-directional SRG-CRD detection: methodology and results

4.1 Design and construction

Here we consider uni-directional cw SRG-CRD experiments that enable reduction of Doppler-broadened linewidths relative to those obtained with the bi-directional cw SRG-CRD spectrometers described in Sects. 3.1 and 3.2 above. We recognise [5] that a bi-directional cw SRG-CRD spectrometer will yield spectra arising from a 1 : 1 superposition of co- and counter-propagating SRG-pump and Stokes (probe) beams with small and large contributions to the Doppler-broadened linewidth, respectively. To overcome this limitation, a uni-directional cw SRG-CRD approach has been projected [5] as a way to eliminate the large Doppler broadening arising in the counter-propagating geometry and to realise the higher-resolution potential of our new cw SRG-CRD spectroscopic technique. This concept has been introduced in Sects. 1.1 and 1.2 and schematically depicted in Fig. 1.

The layout of such a "ring-in-a-ring" intracavity-pumped cw SRG-CRD spectrometer is illustrated in more detail in Fig. 9. Many of its components are in common with those of the linear-ringdown-cavity cw SRG-CRD spectrometer depicted in even more detail in Figs. 4 and 5 but, in the interests of simplicity, some (e.g. pump-laser details, beam-alignment irises and HeNe laser, filters and focusing optics for PD_1 and PD_2, power meter, wavemeter and other laser beam diagnostics) are not portrayed in Fig. 9.

As shown in Fig. 1, and now in more detail on Fig. 9, a rapidly-swept ringdown cavity in the form of a uni-directional four-mirror bow-tie ring (M_5–M_8) is introduced into the four-mirror (M_1–M_4) ring cavity of the pump laser L_P, replacing the previously used linear ringdown cavity (M_5–M_6) in the intracavity-pumped cw SRG-CRD spectrometer configurations shown in Figs. 4, 5, and 7. Ironically, we had used a similar four-mirror ring-form ringdown cavity to reduce optical feedback in early cw SRG-CRD measurements using an external cw Nd:YAG laser that had insufficient power to pump CRD-detectable SRG [6].

Mirrors M_5 and M_6 are identical to those used in the bi-directional linear-cavity cw SRG-CRD spectrometers described in Sects. 2 and 3 and Figs. 4, 5, and 7; they are mounted at similar locations to those of the previous systems. The ring-form ringdown cavity can therefore be placed inside the ring cavity of the SRG-pump laser without major changes in the spatial mode profile of the pump beam. None of the intracavity elements in the pump-laser cavity need to be changed or repositioned, so that the e^{-2} beam diameter of the spatial mode profile of the pump beam at its waist and M_5, M_6 locations remain unchanged.

This is confirmed in Table 1 which summarises beam-overlap simulations [6], for both bi-directional and uni-directional cw SRG-CRD spectrometers that are of interest in Sects. 3 and 4, respectively. The simulated e^{-2} beam diameters of Stokes (probe) and SRG-pump beams at various positions within the Raman-interaction section of the ring-form ringdown cavity have been optimised to achieve good beam overlap and high Raman gain as well as optimal pump-laser operation (see Table 1).

The distance L_R over which the Stokes (probe) beam and the SRG-pump beam are able to overlap and interact inside the ring-form ringdown cavity is ∼29.5 cm (i.e. the M_5–M_6 distance), identical to the interaction length previously used with the linear ringdown cavity. However, L_R is only part of the overall round-trip length L_C of the ring-form ringdown cavity, so that the SRG-pumped power gain contributes only over the interaction length L_R, whereas linear absorption at λ_S occurs over the entire round-trip length L_C, as discussed in the context of (12) in Sect. 1.2 above. The round-trip length L_C of our four-mirror (M_5–M_8) ringdown cavity is ∼92 cm (∼0.33-GHz FSR), with fold angles $\Theta_{856} = \Theta_{567} = 7.0°$ and $\Theta_{678} = \Theta_{785} = 12.3°$. The 29.5-cm effective interaction length L_R therefore comprises ∼32% of the overall round-trip cavity length. The remaining mirrors (M_7, M_8; Los Gatos Research; 0.5-m concave radius, 25.4-mm diameter, and 1° wedge angle of the fused silica substrate) do not need to transmit the SRG-pump radiation at λ_P and so can have very high reflectivity R (∼99.997%) at ∼1.55 μm. For this ring-form ringdown cavity, we measure an empty-cavity ringdown time τ_0 of ∼6.3 μs, corresponding to a net cavity reflectivity R of ∼99.95%, which is consistent with the specified reflectivity (>99.96%) of the Layertec mirrors (M_5, M_6) at normal incidence.

The ring-form ringdown cavity was developed as a monolithic structure, milled out of a solid block of aluminium. This design increases stability and minimises vibrations, as well as avoiding distortions in the cavity structure due to changes of gas-sample pressure. Three of the ringdown mirrors (M_5–M_7) are held in stainless steel optical mounts attached to the monolithic ring-form cavity structure, while the fourth (M_8) is mounted on the same cylindrical low-voltage PZT as in Sect. 3, to allow rapid modulation of the ringdown cavity length. The monolithic ringdown cavity module with its attached mirrors is located and aligned inside the ring cavity of the pump laser L_P, replacing the previously implemented linear ringdown cavity. Fig. 10 shows a photograph of the assembled "ring-in-a-ring" cw SRG-CRD spectrometer, with actual components labeled as in Fig. 9.

Many other aspects of the uni-directional "ring-in-a-ring" cw SRG-CRD spectrometer configuration are as in the system described in detail in the context of Fig. 5 and Sect. 3.1. As in Sect. 3.2, a single-mode fibre designed for ∼1.5 μm (Thorlabs, model P3-SMF28-FC-5) is used to launch Stokes (probe) laser output power of ∼4 mW into the ringdown cavity. The configuration of the "ring-in-a-ring" intracavity-pumped cw SRG-CRD spectrometer uses the same 10-MHz

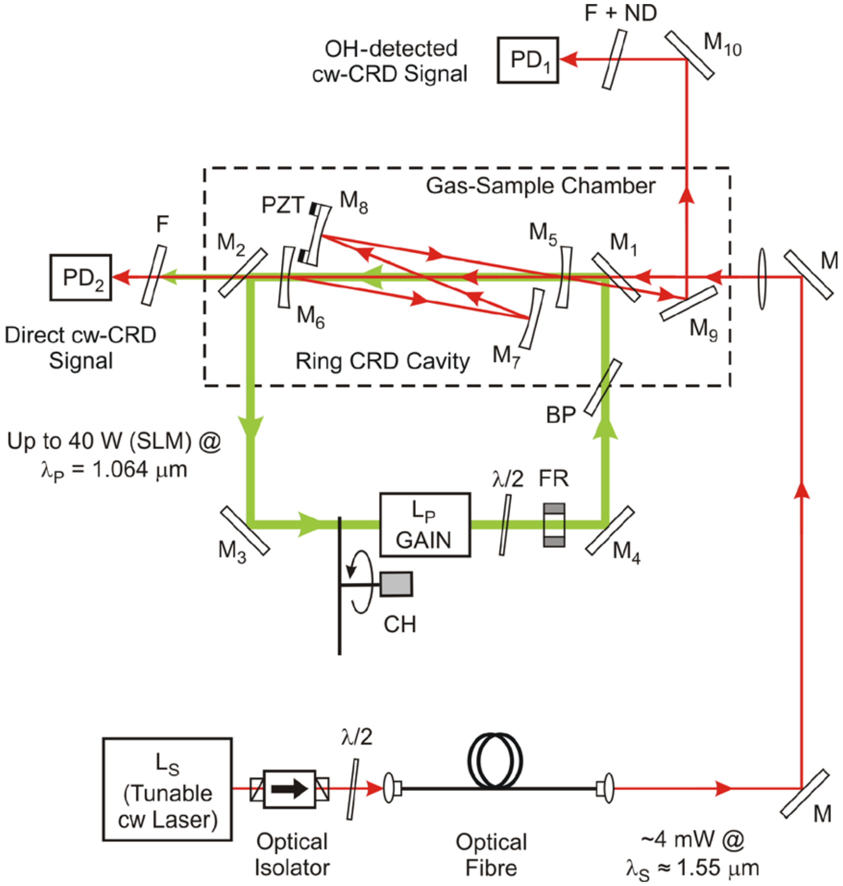

Fig. 9 Detailed layout of a ring-in-a-ring instrument for uni-directional cw SRG-CRD spectroscopy, extending the simplified schematic of Fig. 1. Features not previously shown in Fig. 1 include two photodetectors PD$_1$ and PD$_2$ (for backward- and forward-propagating CRD detection, respectively), specifics of the pump-laser optical diode (BP, FR, λ/2), the tunable cw laser L$_S$ (with associated components for isolation, fibre-optical transmission and spatial filtering, and polarisation-control), and additional beam-steering mirrors (M, M$_9$, M$_{10}$). See text for further details

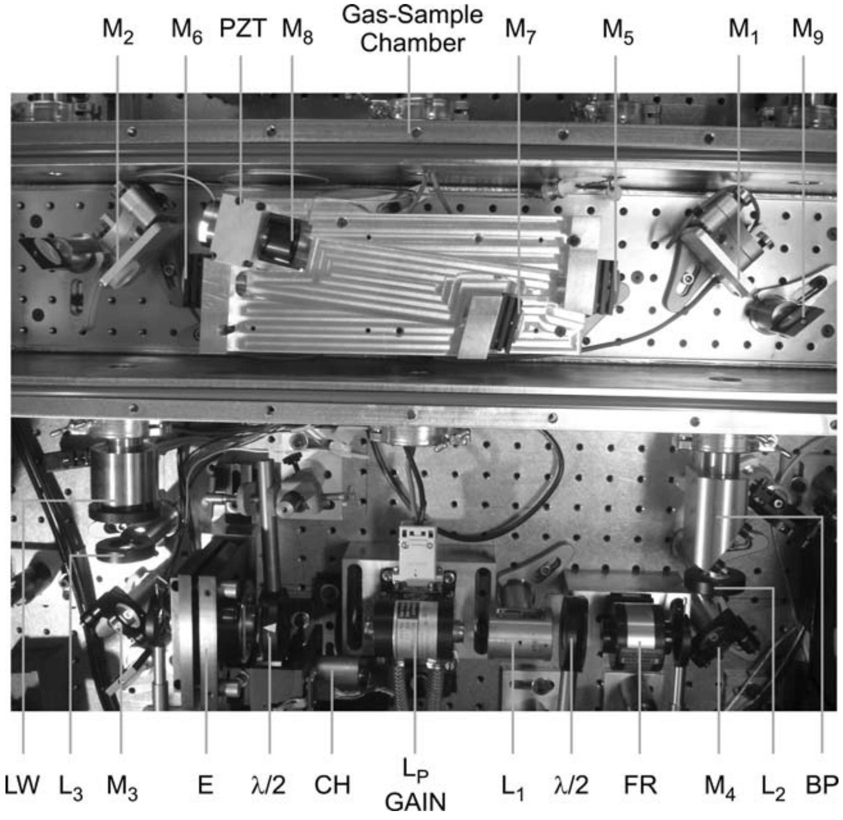

Fig. 10 Photograph of the ring-in-a-ring cw SRG-CRD spectrometer (with the lid of the gas-sample chamber removed), showing various components identified schematically in Figs. 1, 4, and 9. The four-mirror ringdown cavity is formed by a monolithic machined aluminium structure, on which reflectors M$_5$–M$_8$ and the piezoelectric translator PZT are mounted. Various additional components are outside the field of view

low-noise photodetector PD_2 as in Sect. 3 for directly transmitted forward-propagating cw CRD detection, processed by one input channel of the high-performance digitiser. The other digitiser input channel is available to process backward-propagating OH-detected cw CRD signals; these are collected by the same 125-MHz photodetector PD_1 as in Sect. 3, but with a different arrangement as depicted in Fig. 9, via flat turning mirrors M_9 and M_{10} and a Brewster-angle exit window (fused silica with 1° wedge angle, attached to an ISO-K flange vacuum port; not shown in Figs. 9 or 10) from the gas-sample chamber. An alternative use for the second input channel of the digitiser is to reconfigure it to monitor and record the intracavity power of the SRG-pump laser L_P, using the analog power meter output (Newport, model 2832-C), rather than OH-detected cw CRD signals from PD_1.

4.2 Alignment and polarisation characteristics

Exact alignment and optical polarisation characteristics of the ring-form ringdown cavity turn out to be critically important. If the light in the four-mirror ringdown cavity does not propagate within a single plane, then slow oscillatory behaviour can arise in *both* the directly transmitted (forward-propagating) *and* the OH-detected (backward-propagating) cw CRD signals. For example, such slow oscillations are clearly visible in the envelope of the OH-detected cw CRD signal waveform depicted in Fig. 11(a), with non-planar alignment of the four-mirror ring-form ringdown cavity. Fig. 11(b) shows that a higher-amplitude, smoothly decaying OH-detected cw CRD signal waveform is recovered when Stokes (probe) light in the four-mirror ringdown cavity is restored to planar alignment.

Such slow oscillatory effects can be observed when the polarisation of the input Stokes (probe) beam is neither parallel nor orthogonal to the plane(s) of reflection in the ringdown cavity. In a non-planar four-mirror cavity, it is inevitable that the polarisation will be rotated in at least some of the intracavity reflections. Reflection characteristics (reflectivity and shift of phase) of the ringdown-cavity mirrors may be slightly different for p- and s-polarisations, so that successive round-trips may change the Stokes (probe) beam polarisation through a coherent superposition of two ringdown-decay effects (p- and s-polarised) with different ringdown times τ and/or different attenuations when traversing various optical elements before reaching a photodetector. Both forms of polarisation can oscillate inside a non-planar four-mirror ringdown cavity, with a different mirror reflectivity for each polarisation and changes in polarisation accumulating on each intracavity round-trip. Interference of these two ringdown effects gives rise to the observed slow oscillations in both forms (direct and OH-detected) of cw CRD signal waveform. The cw CRD signal waveforms influenced by such slow oscillatory behaviour are not suitable for accurate measurement of ringdown times τ, so that the four-mirror ringdown cavity needs to be aligned to a planar configuration (e.g. by monitoring the OH-detected cw CRD signal on PD_1) to achieve an acceptable outcome as in Fig. 11(b).

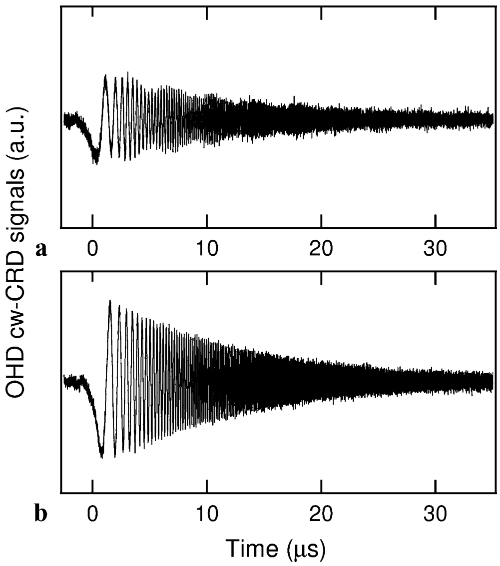

Fig. 11 Optical-heterodyne (OH) detected cw CRD signal waveforms from a ringdown cavity in the form of a four-mirror bow-tie ring (as in Figs. 1, 9, and 10). Slow oscillations in the OH-detected cw CRD signal of trace (**a**) are due to non-planar alignment of the ring-form ringdown cavity and/or imperfect alignment of the linear polarisation of the input Stokes (probe) beam (which should be either parallel or orthogonal to the plane of the ring). Trace (**b**) is the OH-detected cw CRD signal observed after the ring-form ringdown cavity has been precisely aligned to be planar, as is highly desirable for CRD measurements

In addition, the amplitude of the observed slow oscillatory behaviour can be increased or minimised by temporarily placing and rotating a polarising beam-splitter cube in the Stokes (probe) beam (i.e. in front of mirror M_5) incident on a *planar* four-mirror ringdown cavity. These are similar to the observed oscillations in the signal shown in Fig. 11(a), with a *non-planar* four-mirror ringdown cavity. Figure 12(a) depicts such slow oscillations in an OH-detected cw CRD signal waveform, comparable to those for a non-planar ring in Fig. 11(a) but arising from pronounced rotation of the plane of polarisation of the input Stokes (probe) beam relative to the plane of the ring. With less pronounced misalignment of polarisation, both the period and amplitude of the slow oscillations in the signal envelope become longer and weaker, respectively, as shown in Fig. 12(b). These slow oscillations are eliminated under the polarizer-orientation conditions of Fig. 12(c).

It was found impractical to implement a “ring-in-a-ring” cw SRG-CRD spectrometer in a chopper-free dual-ringdown-cavity configuration analogous to that of Sect. 3.2 and Fig. 7. This is because the “ring-in-a-ring” spectrometer exhibited small but troublesome cw CRD baseline os-

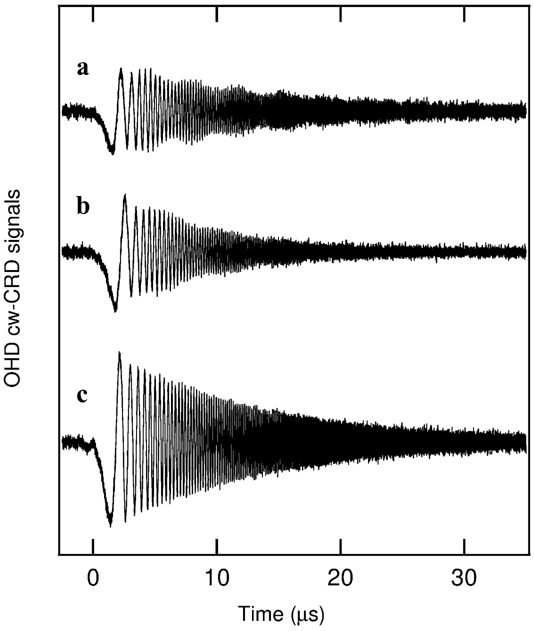

Fig. 12 OH-detected cw CRD signal waveforms of the planar ring-form ringdown cavity for three different alignments of the plane of polarisation of the input Stokes (probe) beam relative to the plane of the ring: (**a**) oscillations comparable to those in Fig. 11(a), arising from pronounced misalignment of polarisation; (**b**) reduction of oscillations with less pronounced misalignment of polarisation; (**c**) minimisation of oscillations with optimal alignment of polarisation

cillations which prevented exact cw CRD background subtraction using a second zero-I_P reference ringdown cavity (which did not exhibit the same oscillations). These oscillations, at ~16 GHz (~0.54 cm^{-1}), correspond to a free-space optical pathlength of ~9.2 mm, or a thickness of ~6.3 mm in BK7 glass or fused silica; they are independent of gas-fill or SRG-pumping and are probably due to an unidentified persistent interference effect in a mirror or lens associated with the ring-form ringdown cavity. It was therefore found necessary to retain the intracavity chopper as an essential element in acquiring, processing and analysing experimental cw SRG-CRD spectroscopic data. To increase the duty factor and data rate of the system, it was found possible to increase the chopper frequency from 40 Hz to 100 Hz, without impairing stable quasi-cw operation of the pump ring laser.

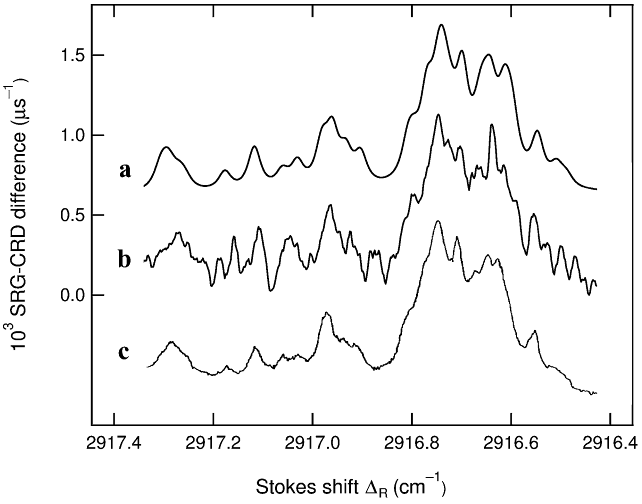

Fig. 13 SRG spectra for the 2916.5-cm^{-1} ν_1 Raman band of $^{12}CH_4$ gas at 296 K. Trace (**a**) is a simulated rovibrational band contour. Trace (**b**) is a cw SRG-CRD difference spectrum, recorded at $p = 200$ Torr using the uni-directional ring-in-a-ring cw SRG-CRD spectrometer with co-propagating SRG-pump and CRD-resonant Stokes beams. Trace (**c**) is a comparable conventional SRG spectrum at $p = 150$ Torr experimentally recorded by Owyoung [20]. See text for further details

4.3 Performance and spectroscopic results

Three spectra of the 2916.5-cm^{-1} ν_1 fundamental rovibrational Raman band of $^{12}CH_4$ gas at 296 K, each plotted as a function of the Stokes shift $\Delta_R = (\omega_P - \omega_S)$, are presented in Fig. 13. Trace (a) is a predicted rovibrational band contour, simulated with the best available model by Lolck [81], relative intensities provided by Owyoung et al. [66, 67] and a Voigt line profile with FWHM Gaussian and Lorentzian contributions of $\Delta\nu_D = 0.009$ cm^{-1} and $\Delta\nu_C = 0.028$ cm^{-1}, respectively. The former ($\Delta\nu_D$) is appropriate for a uni-directional ringdown cavity with co-propagating SRG-pump and Stokes (probe) beams as in Figs. 1 and 9, while the latter ($\Delta\nu_C$) corresponds to the pressure broadening expected with $p = 200$ Torr, the $^{12}CH_4$ pressure in the experimental cw SRG-CRD difference spectrum presented in Fig. 13(b). The third trace, in Fig. 13(c), is a conventional optically detected cw SRG spectrum of the same band of $^{12}CH_4$ gas at $p = 150$ Torr, as reported by Owyoung [20].

The experimental cw SRG-CRD difference spectrum in Fig. 13(b) comprises ~450 $\langle\langle\tau_P^{-1}\rangle - \langle\tau_B^{-1}\rangle\rangle$ data points, in each of which the intracavity chopper has been used to subtract average ringdown rates $\langle\tau_B^{-1}\rangle$ from $\langle\tau_P^{-1}\rangle$ for situations without and with pump, respectively, employing a step size of ~5.5 × 10^{-4} nm (~2.3 × 10^{-3} cm^{-1}; ~70 MHz) and a total recording time of ~13 hours. The spectrum in Fig. 13(b) is the grand average of 6 distinct $(\langle\tau_P^{-1}\rangle - \langle\tau_B^{-1}\rangle)$ difference spectra [6], each digitally smoothed (using a Savitzky–Golay moving-window polynomial method [110–112] similar to that employed in Sects. 3.1 and 3.2). Each $(\langle\tau_P^{-1}\rangle - \langle\tau_B^{-1}\rangle)$ difference spectrum is in turn determined from $(n \times m) = 1024$ pairs of without- or with-pump rapidly-swept CRD signal waveforms, comprising m $(= 16)$ groups of average $\langle\tau_B^{-1}\rangle$ or $\langle\tau_P^{-1}\rangle$ values, each evaluated by a Levenberg–Marquardt exponential-decay-model fit [107–109] to n $(= 64)$ individual directly transmitted cw CRD waveforms, subject to rejection whenever its τ_B^{-1} or τ_P^{-1} value differs from the corresponding mean by more than 2 standard deviations (which typically eliminated ~5% of the raw cw CRD waveforms). As before, the SRG-pump laser wavelength λ_P is set at 1064.42 nm, the Stokes (probe) laser wavelength λ_S is tuned in the vicinity of 1544 nm, and the frequency scales of the cw SRG-CRD difference spectrum in Fig. 13(b) and of the six contributing $(\langle\tau_\mathrm{P}^{-1}\rangle - \langle\tau_\mathrm{B}^{-1}\rangle)$ cw SRG-CRD difference spectra [6] are linearised and calibrated via known features in the ∼1544-nm absorption spectrum of $^{12}\mathrm{CH}_4$ [86, 87] and the corresponding $^{12}\mathrm{CH}_4$ swept-frequency CRD absorption spectrum recorded in Fig. 3.

Prior to digital smoothing, the noise-limited sensitivity for each of the six cw SRG-CRD difference spectra $(\langle\tau_\mathrm{P}^{-1}\rangle - \langle\tau_\mathrm{B}^{-1}\rangle)$ is $\mathrm{MDLG} = 1.6 \times 10^{-8}\ \mathrm{cm}^{-1}$; with a measurement interval of $t_\mathrm{M} = 16.5$ s per data point, the normalised MDLG_N value is $6.4\ \times 10^{-8}\ \mathrm{cm}^{-1}\ \mathrm{Hz}^{-1/2}$ [6]. This MDLG_N value applies also to the corresponding grand-average $\langle\langle\tau_\mathrm{P}^{-1}\rangle - \langle\tau_\mathrm{B}^{-1}\rangle\rangle$ cw SRG-CRD difference spectrum from which Fig. 13(b) is derived (after digital smoothing); its un-normalised noise-limited sensitivity is therefore $\mathrm{MDLG} = 6.5 \times 10^{-9}\ \mathrm{cm}^{-1}$—a factor of $6^{-1/2}$ finer than for the six individual $(\langle\tau_\mathrm{P}^{-1}\rangle - \langle\tau_\mathrm{B}^{-1}\rangle)$ cw SRG-CRD difference spectra [6].

The experimental cw SRG-CRD difference spectrum recorded in Fig. 13(b) for the 2916.5-$\mathrm{cm}^{-1}\,\nu_1$ fundamental rovibrational Raman band of $^{12}\mathrm{CH}_4$ gas compares satisfactorily with the simulated and optically detected SRG spectra in traces (a) and (c) of Fig. 13, respectively. Apparent spurious peaks that were noted in the context of the upper traces Figs. 6(b) and 8(b) are now less prominent, which is consistent with the increased extent of signal-averaging used to extract the cw SRG-CRD difference spectrum in Fig. 13(b). However, those at $\Delta_\mathrm{R} \approx 2916.90\ \mathrm{cm}^{-1}$ and $\Delta_\mathrm{R} \approx 2916.85\ \mathrm{cm}^{-1}$ (tentatively attributed in Sect. 3 to background-subtraction noise) still persist and an unexpected narrow peak is evident at $\Delta_\mathrm{R} = 2916.64\ \mathrm{cm}^{-1}$ but is also considered to be spurious and due to background-subtraction noise. As noted in Sects. 3.1.2 and 3.2.2, such effects are minimised by resetting λ_S to its starting value before incrementing it to the next point in a spectroscopic scan. However, this minimisation procedure becomes less accurate at lower gas-sample pressures when absorption features become narrower.

The most significant outcome of Fig. 13(b), which is recorded uni-directionally with co-propagating pump and Stokes beams, is that it exhibits a much higher resolution than that in the upper traces Figs. 6(b) and 8(b), which arise from a bidirectional superposition of pump and Stokes beams that results in greater net Doppler broadening. This is consistent with our expectation [5], as explained in Sect. 1 above. Moreover, the narrower Doppler width is borne out by the simulation in Fig. 13(a) and the optically detected SRG spectrum in Fig. 13(c).

Further confirmation of this Doppler-broadening effect has been obtained by adjusting the half-wave plate ($\lambda/2$) next to the Faraday rotator FR inside the pump laser ring cavity (see Fig. 4) to reverse the direction of propagation of the pump-laser radiation (i.e. such that the pump-laser radiation is now propagating clockwise inside the ring laser cavity, rather than anti-clockwise). Reversal of the intracavity SRG-pump laser beam propagation in this way establishes SLM operation with similar cw intracavity pump power levels as before and an increased Doppler width corresponding to counter-propagating SRG-pump and Stokes beams is expected. A corresponding experimental cw SRG-CRD spectra of the ν_1 rovibrational Raman band of $^{12}\mathrm{CH}_4$ gas with $p = 200$ Torr and $T = 296$ K is presented in Fig. 14(a); it is recorded under similar conditions to those used to record Fig. 13(b), apart from the reversal of the pump-beam direction such that SRG-pump and Stokes (probe) beams are counter-propagating. Figure 14(a) is an average of two $(\langle\tau_\mathrm{P}^{-1}\rangle - \langle\tau_\mathrm{B}^{-1}\rangle)$ difference spectra [6] with a total recording time of ∼4.3 hours and $\mathrm{MDLG} = 1.6 \times 10^{-8}\ \mathrm{cm}^{-1}$, prior to digital smoothing. Fig. 14(b) depicts a simulated SRG spectrum for counter-propagating SRG-pump and Stokes beams, with a 5.4-fold increase of $\Delta\nu_\mathrm{D}$ to 0.049 cm^{-1} compared to 0.009 cm^{-1} in Fig. 13(c). It is evident that the experimental and simulated SRG spectra are in satisfactory agreement, with much lower resolution than in the co-propagating case (Fig. 13) and the bi-directional case (Figs. 6 and 8) [5]. Indeed, the increased Doppler broadening in the unfavourable counter-propagating case makes the characteristic dip at $\Delta_\mathrm{R} \approx 2916.7\ \mathrm{cm}^{-1}$ barely discernible.

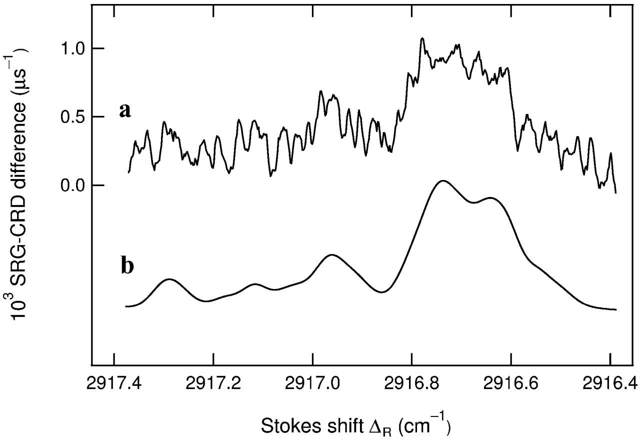

Fig. 14 Cw SRG-CRD spectra with counter-propagating SRG-pump and CRD-resonant Stokes beams: (**a**) observed and (**b**) simulated, with much more pronounced Doppler broadening than for their co-propagating counterparts in Figs. 13(b) and 13(a), respectively. See text for further details

5 Concluding discussion

This paper presents a comprehensive account of a new stimulated-Raman-gain spectroscopic technique, in which rapidly-swept cavity-ringdown detection is used to monitor the transfer of optical power from coherent cw pump radiation at a fixed frequency ω_P (or wavelength λ_P) is transferred to coherent cw Stokes radiation at a tunable frequency ω_S (or wavelength λ_S) when the difference frequency $(\omega_P - \omega_S)$ is scanned through successive Raman transition frequencies Δ_R in gas-phase molecules of interest. This SRG-CRD technique takes advantage of the high sensitivity of CRD spectroscopy, but such experiments with narrowband cw lasers are still a major challenge as the Raman gain tends to be extremely weak at available pump irradiances [5, 6]. It is necessary to maximise the pump irradiance I_P by using the intracavity field of a Nd:YAG ring laser and locating the ringdown cavity (which is probed by the Stokes radiation) inside the ring cavity of that pump laser. Moreover, it is vital (but far from trivial) to optimise the overlap of the SRG-pump and Stokes (probe) beams with irradiance as high as is practicable over their entire pathlength within the ringdown cavity. The feasibility of such a SRG-CRD-spectroscopic approach has been verified by investigating the 2916.5-cm^{-1} ν_1 fundamental rovibrational Raman band of ^{12}CH$_4$ gas at 296 K and pressures p down to 200 Torr. Salient outcomes of our paper are itemised below.

- The theoretical and experimental background to cw SRG spectroscopy [3, 4, 8–20] has been surveyed in Sect. 1.1, clarifying a number of potentially confusing issues.
- The strategy of combining cw SRG spectroscopy [4, 19, 20] with CRD detection [1, 2], particularly in its rapidly-swept manifestations [25–28, 88, 89], has been outlined in Sect. 1.2, which addresses crucial experimental considerations. A significant phenomenological expectation is that SRG-CRD signals will appear as a seemingly unusual *increase* in ringdown time τ, compared to the usual loss-induced *decrease* in τ that pertains to CRD absorption spectroscopy. This SRG-induced prolongation of τ in the context of cw SRG-CRD spectroscopy is analogous to the limiting case of a cw Raman laser oscillator [29–56], where high-I_P Raman gain can increase τ markedly.
- The relevant infrared and Raman spectroscopy of CH$_4$ gas has been surveyed in Sect. 1.3. It is shown that, with a Nd:YAG pump-laser wavelength $\lambda_P \approx 1064.4$ nm, SRG-CRD spectra of the Q branch in the ν_1 Raman band of ^{12}CH$_4$ gas, with Stokes shifts $\Delta_R = 2916.4$–2917.4 cm^{-1}, requires the Stokes (probe) laser wavelength to be scanned in the vicinity of $\lambda_S \approx 1543.5$–1543.8 nm. Linear absorption in this region (see Fig. 2) is weak but still sufficiently pronounced (see Fig. 3) to provide a dominant background contribution [86, 87] to cw SRG-CRD spectra of ^{12}CH$_4$ gas, on the basis of the known Raman cross-section and linewidth data [13] at available pump irradiances I_P. Efficient extraction of the very small Raman signal with acceptable spectroscopic precision, detection sensitivity, and SNR requires background-subtraction measures that are far from trivial.
- Detailed descriptions have been given in Sect. 3 of two cw SRG-CRD spectrometers with a linear two-mirror ringdown cavity inside the ring cavity of the pump laser: one (see Sect. 3.1 and Fig. 5) using an intracavity pump-beam chopper for background subtraction; the other (see Sect. 3.2 and Fig. 7) adopting a chopper-free dual-ringdown-cavity approach to background subtraction. Corresponding SRG-CRD difference spectra for the ν_1 Raman band of ^{12}CH$_4$ gas have been recorded (see Figs. 6 and 8, respectively) with noise-limited sensitivities MDLG$_N$ $= 5 \times 10^{-8}$ cm^{-1} Hz$^{-1/2}$ and 2.6 $\times 10^{-8}$ cm^{-1} Hz$^{-1/2}$, respectively, and satisfactorily compared with Voigt-profile simulations, based on a bi-directional superposition of SRG-CRD signals arising from co- and counter-propagating SRG-pump and Stokes (probe) beams.
- To overcome the above excessive Doppler-broadening effects, a uni-directional “ring-in-a-ring” cw SRG-CRD spectrometer has been developed with a four-mirror ring-form ringdown cavity inside the ring cavity of the pump laser and an intracavity pump-beam chopper for background subtraction (see Sect. 4 and Figs. 1, 9, and 10). This yields a SRG-CRD difference spectrum for the ν_1 Raman band of ^{12}CH$_4$ gas (see Fig. 13) with MDLG$_N$ $=$ 6.4×10^{-8} cm^{-1} Hz$^{-1/2}$; the experimental spectrum is more highly resolved and is satisfactorily compared with Voigt-profile simulations.

The objective of this project at its outset was to exploit sensitive CRD detection as a novel means of recording high-resolution SRG spectra of gas-phase molecules [5, 6]. Our intention has been to use readily available, low-cost cw SLM solid-state lasers (e.g. a cw Nd:YAG laser as SRG-pump and communications-band tunable diode laser as Raman Stokes and CRD-probe source for ^{12}CH$_4$ gas) which promised to be less elaborate and expensive than the large, expensive SLM gas-phase and dye lasers traditionally used for cw optically detected SRG spectroscopy [20, 66, 67]. This objective has been attained to the extent demonstrated in this paper. However, in terms of prospects for widespread applications, severe limitations are imposed by the complexity of the necessary instrumentation and the degree of experimental difficulty (particularly that imposed by the strength of the underlying linear absorption background in ^{12}CH$_4$.

Our current SRG-CRD instrumentation to record high-resolution cw SRG spectra of gases therefore appears to be less convenient (and inferior in terms of SNR and spectroscopic resolution) than the traditional optically detected approach. For example, it has not been feasible for our cw SRG-CRD approach to match the widely published (e.g. see Fig. 16 of [20], Fig. 4.14 of [60], Fig. 2 of [66, 67], and Fig. 2 of [70]) cw SRG spectrum of the Q branch in the ν_1 band of ^{12}CH$_4$ gas at $p = 35$ Torr and 297 K, although the experimental time taken to record that iconic spectrum has never been reported. The closest that our cw SRG-CRD experiments have come is presented in Fig. 13(b) for $^{12}CH_4$ gas at $p = 200$ Torr, which compares with an optically detected cw SRG spectrum [20] shown in Fig. 13(c) for $^{12}CH_4$ gas at $p = 150$ Torr.

Our novel cw SRG-CRD spectroscopic approach is derived from the confluence of two forms of laser spectroscopy, namely, cw CRD spectroscopy and cw SRG spectroscopy. It extends cw-CRD spectroscopy for the first time from its conventional optical-absorption mode of operation into the regime of coherent Raman spectroscopy. Various possible instrumental developments have been contemplated to enhance the sensitivity (and consequent utility) of cw SRG-CRD spectroscopy beyond what has been achieved so far. Specific prospects are outlined below.

- The most obvious improvement would be to increase the irradiance I_P of the cw SRG-pump beam (and hence the integrated Raman power-gain factor $\langle g_R \ I_P \ L_R\rangle$ for the Stokes beam) throughout the ringdown cavity. As explained in Sect. 1.1, these have been maximised in the present instrument by using a Nd:YAG ring laser with an intracavity ringdown cavity. The intracavity pump power could be increased by introducing another diode-pumped Nd:YAG amplifier head, which might also enable additional birefringence compensation. Such modification would require a new design for the ring cavity of the pump laser (e.g. a longer resonator round-trip length) taking account of its likely thermal lensing characteristics and placement of intracavity elements such as lenses and the ringdown-cavity mirrors. Moreover, the extent of any such improvement would depend on control of saturation effects and SLM stability that limited the maximum SLM intracavity pump power that was attainable with a single diode-pumped Nd:YAG amplifier head, as discussed in Sect. 2.2. Furthermore, special-quality coatings for the ringdown cavity mirrors (M_5, M_6), with higher reflectivity at λ_S ($\sim$1550 nm) and lower loss at λ_P ($\sim$1064 nm), might be procured to improve the detection sensitivity of the SRG-CRD system.
- Another possible way to increase the intracavity SRG-pump irradiance I_P of the cw SRG-pump beam (and hence the Raman gain factor $\langle g_R \ I_P \ L_R\rangle$) could be to adopt a quasi-cw approach to SRG-pumping. For instance, long-pulse (with an I_P-plateau of $\sim$100-µs duration), low-repetition-rate ($\sim$50 Hz) Q-switched operation of the Nd:YAG ring laser might be a means (e.g. by using a suitable electro-optic modulator) of attaining a factor-of-100 increase in the effective value of I_P over the duration of each SRG-pumped CRD decay waveform.
- A substantial improvement in the Raman gain parameter g_R is expected by using shorter-wavelength SRG-pump and Stokes (probe) lasers, given the λ^{-4} dependence of Raman scattering cross-sections. Moreover, many gas-phase molecules (e.g. alkanes, alkenes, alkynes, …) are likely to display less pronounced background interference from linear absorption if the tunable Stokes (probe) wavelength is in the visible or near-ultraviolet rather than the near-infrared (where rovibrational overtone spectra may still be too prominent to avoid masking of cw SRG-CRD spectra of interest). However, such shorter-wavelength SRG-CRD excitation would be likely to involve more elaborate, expensive high-power lasers than are used in this paper.
- We have contemplated a more advanced, dual-channel implementation of a chopper-free "ring-in-a-ring" cw SRG-CRD spectrometer [6], in which separate CRD photodetectors simultaneously monitor co- and counter-propagating CRD waveforms for a gas-phase sample at low pressures and associated fitted ringdown rates τ^{-1} are subtracted to yield spectroscopic features with a lineshape of second-derivative style, comprising a narrow peak with a broader inverted pedestal; these correspond respectively to Doppler widths for co- and counter-propagating pump and Stokes beams and the linear-absorption background is automatically subtracted and nulled.
- We have also considered the feasibility of a cw SRG-CRD technique to detect pure rotational Raman spectra [115], given that many molecules have cross-sections for pure rotational Raman scattering that are typically $\sim$3 orders of magnitude larger than those for rovibrational Raman scattering. A major challenge is to separate the SRG-pump and Stokes (probe) beams, since the difference between λ_P and λ_S is now much less (tens of cm^{-1}) in the case of pure rotational Raman spectra than in the rovibrational Raman case. A possible cw SRG-CRD spectrometer design, proposed [6] to realise this objective, is based on a 3-mirror rapidly-swept ringdown cavity and orthogonally polarised SRG-pump and Stokes (probe) beams; mirrors at large angle of incidence can have high reflectivity for one direction of light polarisation for the Stokes (probe) beam and high transmission for an orthogonally polarised SRG-pump beam.

In conclusion, we have achieved what we believe to be the first-ever cavity-ringdown realisation of coherent Raman spectroscopy [5, 6], thereby broadening the scope of CRD techniques for spectroscopic sensing and complementing conventional forms of SRG spectroscopy. Our approach is characterised by an unusual prolongation of ringdown time τ, associated with the Raman gain process that is detected. Development of proof-of-principle SRG CRD spectrometer designs has depended on all-solid-state cw laser instrumentation and ringdown cavities (probed by tunable Stokes radiation at wavelength λ_S) located inside the ring cavity of a SRG-pump laser (operating at fixed wavelength λ_P). The application of this cw SRG-CRD approach to the

ν_1 Raman band of $^{12}CH_4$ gas, with Stokes shifts Δ_R in the vicinity of ∼2916.5 cm^{-1}, has been complicated by the relative strength of underlying linear absorption and the need to subtract this background in order to measure SRG-CRD difference spectra that may be compared with SRG spectra obtained by conventional optically detected techniques.

Acknowledgements We acknowledge financial support from Macquarie University, the Australian Research Council, and the Australian Department of Education, Science and Technology.

References

1. K.W. Busch, M.A. Busch (eds.), *Cavity-Ringdown Spectroscopy—An Ultratrace-Absorption Measurement Technique*. ACS Symposium Series, vol. 720 (American Chemical Society, Washington, 1999)
2. G. Berden, R. Peeters, G. Meijer, Int. Rev. Phys. Chem. **19**, 565 (2000)
3. A.B. Harvey (ed.), *Chemical Applications of Nonlinear Raman Spectroscopy* (Academic Press, New York, 1981)
4. P. Esherick, A. Owyoung, Adv. Infrared Raman Spectrosc. **9**, 130 (1982)
5. F.V. Englich, Y. He, B.J. Orr, Appl. Phys. B **83**, 1 (2006)
6. F.V. Englich, New approaches to cavity ringdown laser spectroscopy. Ph.D. Thesis, Macquarie University, Sydney, 2007
7. F.V. Englich, Y. He, B.J. Orr, Stimulated Raman gain spectroscopy with continuous-wave cavity ringdown detection, in *Conference on Lasers & Electro-Optics/Quantum Electronics & Laser Science Conference, and Photonic Applications Systems Technologies*. OSA Technical Digest Series (CD) (Optical Society of America, 2007), paper CWE1. http://www.opticsinfobase.org/abstract.cfm?URI=CLEO-2007-CWE1
8. P.N. Butcher, D. Cotter, *The Elements of Nonlinear Optics* (Cambridge University Press, Cambridge, 1990)
9. Y.R. Shen, *The Principles of Nonlinear Optics* (Wiley, New York, 1984)
10. R.W. Boyd, *Nonlinear Optics*, 2nd edn. (Academic Press, San Diego, 2003)
11. W.R. Trutna, R.L. Byer, Appl. Opt. **19**, 301 (1980)
12. D. Cotter, D.C. Hanna, R. Wyatt. Appl. Phys. **8**, 333 (1975)
13. A. Kazzaz, S. Ruschin, I. Shoshan, G. Ravnitsky, IEEE J. Quantum Electron. **30**, 3017 (1994)
14. W. Kaiser, M. Maier, Stimulated Rayleigh, Brillouin, Raman spectroscopy, in *Laser Handbook*, vol. 2, ed. by F.T. Arecchi, E.O. Schultz-Dubois (North-Holland, Amsterdam, 1972), pp. 1077–1150, Chap. E2
15. M. Maier, Appl. Phys. **11**, 209 (1976)
16. A. Penzkofer, A. Laubereau, W. Kaiser, Prog. Quantum Electron. **6**, 55 (1979)
17. H.W. Schrötter, H.W. Klöckner, Raman scattering cross sections in gases and liquids, in *Raman Spectroscopy of Gases and Liquids*, ed. by A. Weber. Topics in Current Physics Series, vol. 11 (Springer, Berlin, 1979), pp. 123–166, Chap. 4
18. J. Reintjes, M. Bashkansky, Stimulated Raman and Brillouin scattering, in *Handbook of Optics, vol. IV, Fiber Optics and Nonlinear Optics*, ed. by M. Bass, J.M. Enoch, E.W. Van Stryland, W.L. Wolfe (McGraw-Hill, New York, 2001), pp. 18.1–18.61, Chap. 18
19. A. Owyoung, IEEE J. Quantum Electron. **QE-14**, 192 (1978)
20. A. Owyoung, CW stimulated Raman spectroscopy, in *Chemical Applications of Nonlinear Raman Spectroscopy*, ed. by A.B. Harvey (Academic Press, New York, 1981), pp. 281–320, Chap. 7
21. A.C. Eckbreth, P. Schreiber, Coherent anti-Stokes Raman spectroscopy (CARS): application to combustion and gas-phase diagnostics, in *Chemical Applications of Nonlinear Raman Spectroscopy*, ed. by A.B. Harvey (Academic Press, New York, 1981), pp. 28–87, Chap. 2
22. E.S. Yeung, Applications of inverse Raman spectroscopy, in *Chemical Applications of Nonlinear Raman Spectroscopy*, ed. by A.B. Harvey (Academic Press, New York, 1981), pp. 172–204, Chap. 4
23. J.J. Barrett, Photoacoustic Raman spectroscopy of gases, in *Chemical Applications of Nonlinear Raman Spectroscopy*, ed. by A.B. Harvey (Academic Press, New York, 1981), pp. 89–169, Chap. 3
24. G.D. Boyd, W.D. Johnston, I.P. Kaminow, IEEE J. Quantum Electron. **QE-5**, 203 (1969)
25. Y. He, B.J. Orr, Chem. Phys. Lett. **319**, 131 (2000)
26. Y. He, B.J. Orr, Chem. Phys. Lett. **335**, 215 (2001)
27. Y. He, B.J. Orr, Appl. Phys. B **75**, 267 (2002)
28. Y. He, B.J. Orr, Appl. Phys. B **85**, 355 (2006)
29. J.K. Brasseur, K.S. Repasky, J.L. Carlsten, Opt. Lett. **23**, 367 (1998)
30. K.S. Repasky, J.K. Brasseur, L. Meng, J.L. Carlsten, J. Opt. Soc. Am. B **15**, 1667 (1998)
31. J.K. Brasseur, P.A. Roos, K.S. Repasky, J.L. Carlsten, J. Opt. Soc. Am. B **16**, 1305 (1999)
32. P.A. Roos, J.K. Brasseur, J.L. Carlsten, Opt. Lett. **24**, 1130 (1999)
33. L.S. Meng, K.S. Repasky, P.A. Roos, J.L. Carlsten, Opt. Lett. **25**, 472 (2000)
34. L.S. Meng, P.A. Roos, K.S. Repasky, J.L. Carlsten, Opt. Lett. **26**, 426 (2001)
35. J.C. Bienfang, W. Rudolph, P.A. Roos, L.S. Meng, J.L. Carlsten, J. Opt. Soc. Am. B **19**, 1318 (2002)
36. L.S. Meng, P.A. Roos, J.L. Carlsten, Opt. Lett. **27**, 1226 (2002)
37. J.K. Brasseur, R.F. Teehan, P.A. Roos, B. Soucy, D.K. Neumann, J.L. Carlsten, Appl. Opt. **43**, 1162 (2004)
38. E.P. Ippen, Appl. Phys. Lett. **16**, 303 (1970)
39. S.X. Qiang, J.B. Snow, H.M. Tzeng, R.K. Chang, Science **231**, 486 (1986)
40. H.B. Lin, A.J. Campillo, Phys. Rev. Lett. **73**, 2440 (1994)
41. H.B. Lin, A.J. Campillo, Opt. Commun. **133**, 287 (1997)
42. A.S. Grabitchov, V.A. Lisinetskii, V.A. Orlovich, M. Schmitt, R. Maksimenka, W. Kiefer, Opt. Lett. **29**, 2524 (2004)
43. A.A. Demidovich, A.S. Grabitchov, V.A. Lisinetskii, V.N. Burakevich, V.A. Orlovich, W. Kiefer, Opt. Lett. **30**, 1701 (2005)
44. H.M. Pask, Opt. Lett. **30**, 2454 (2005)
45. P. Dekker, H.M. Pask, D.J. Spence, J.A. Piper, Opt. Express **15**, 7038 (2007)
46. J.A. Piper, H.M. Pask, IEEE J. Sel. Top. Quantum Electron. **13**, 692 (2007)
47. H. Rong, R. Jones, A. Liu, O. Cohen, D. Hak, A. Fang, M. Paniccia, Nature **433**, 725 (2005)
48. H. Rong, S. Xu, Y.-H. Kuo, V. Sih, O. Cohen, O. Raday, M. Paniccia, Nat. Photon. **1**, 232 (2007)
49. E.M. Dianov, A.M. Prokhorov, IEEE J. Sel. Top. Quantum Electron. **6**, 1022 (2000)
50. O. Boyraz, B. Jalali, Opt. Express **12**, 5269 (2004)
51. S.M. Spillane, T.J. Kippenberg, K.J. Vahala, Nature **415**, 621 (2002)
52. B. Min, T.J. Kippenberg, K.J. Vahala, Opt. Lett. **28**, 1507 (2003)
53. T.J. Kippenberg, S.M. Spillane, B. Min, K.J. Vahala, IEEE J. Sel. Top. Quantum Electron. **10**, 1219 (2004)
54. I.S. Grudinin, L. Maleki, Opt. Lett. **32**, 166 (2007)
55. I.S. Grudinin, L. Maleki, J. Opt. Soc. Am. B **25**, 594 (2008)
56. A.A. Savchenkov, A.B. Matsko, M. Mohageg, L. Maleki, Opt. Lett. **32**, 497 (2007)

57. A.B. Matsko, A.A. Savchenkov, L. Maleki, Opt. Commun. **260**, 662 (2006)
58. J.W. Nibler, J.J. Yang, Ann. Rev. Phys. Chem. **38**, 349 (1987)
59. R.J.H. Clark, R.E. Hester (eds.), *Advances in Non-linear Spectroscopy*. Advances in Spectroscopy Series, vol. 15 (Wiley, New York, 1988)
60. M.D. Levenson, S.S. Kano, *Introduction to Nonlinear Laser Spectroscopy* (Academic Press, San Diego, 1988)
61. H.W. Schrötter, H. Berger, J.P. Boquillon, B. Lavorel, G. Millot, J. Raman Spectrosc. **21**, 781 (1990)
62. W.J. Jones, Can. J. Phys. **78**, 327 (2000)
63. H.W. Schrötter, Raman spectra of gases, in *Handbook of Raman Spectroscopy*, ed. by I.R. Lewis, H.G.M. Edwards (Dekker, New York, 2001), pp. 307–348
64. H. Berger, J. Mol. Spectrosc. **66**, 55 (1977)
65. S. Broderson, High-resolution rotational-vibrational Raman spectroscopy, in *Raman Spectroscopy of Gases and Liquids*, ed. by A. Weber. Topics in Current Physics Series, vol. 11 (Springer, Berlin, 1979), pp. 7–69, Chap. 2
66. A. Owyoung, C.W. Patterson, R.S. McDowell, Chem. Phys. Lett. **59**, 156 (1978)
67. A. Owyoung, C.W. Patterson, R.S. McDowell, Chem. Phys. Lett. **61**, 636 (1979)
68. A. Owyoung, High resolution coherent Raman spectroscopy of gases, in *Laser Spectroscopy IV*, ed. by H. Walther, K.W. Rothe. Springer Series in Optical Sciences, vol. 21 (Springer, Berlin, 1979), pp. 175–187
69. J.J. Valentini, P. Esherick, A. Owyoung, Chem. Phys. Lett. **75**, 590 (1980)
70. P. Esherick, A. Owyoung, High resolution inverse Raman and Raman gain spectroscopy, in *Non-Linear Raman Spectroscopy and Its Chemical Applications*, ed. by W. Kiefer, D.A. Long (Reidel, Dordrecht, 1982), pp. 499–517
71. H.W. Schrötter, H. Frunder, H. Berger, J.-P. Boquillon, B. Lavorel, G. Millot, High resolution CARS and inverse Raman spectroscopy, in *Advances in Non-linear Spectroscopy*, ed. by R.J.H. Clark, R.E. Hester. Advances in Spectroscopy Series, vol. 15, (Wiley, New York, 1988), pp. 97–147, Chap. 3
72. D. Bermejo, J. Santos, P. Cancio, J. Mol. Spectrosc. **156**, 15 (1992)
73. J. Santos, P. Cancio, J.L. Domenech, J. Rodriguez, D. Bermejo, Laser Chem. **12**, 53 (1992)
74. D. Pieroni, J.-M. Hartmann, F. Chaussard, X. Michaut, T. Gabard, R. Saint-Loup, H. Berger, J.-P. Champion, J. Chem. Phys. **112**, 1335 (2000)
75. M.A. Henesian, L. Kulevskii, R.L. Byer, R.L. Herbst, Opt. Commun. **18**, 225 (1976)
76. M.A. Henesian, L. Kulevskii, R.L. Byer, J. Chem. Phys. **65**, 5530 (1976)
77. D.N. Kozlov, A.M. Prokhorov, V.V. Smirnov, J. Mol. Spectrosc. **77**, 21 (1979)
78. J.-P. Boquillon, R. Bergier, Appl. Phys. **18**, 195 (1979)
79. E. Gustafson, J. McDaniel, R. Byer, IEEE J. Quantum Electron. **17**, 2258 (1981)
80. H. Frunder, D. Illig, H. Finsterhölzl, H.W. Schrötter, B. Lavorel, G. Roussel, J.C. Hilico, J.P. Champion, G. Pierre, G. Poussigue, E. Pascaud, Chem. Phys. Lett. **100**, 110 (1983)
81. J.-E. Lolck, Chem. Phys. Lett. **106**, 143 (1984)
82. R.S. McDowell, C.W. Patterson, J. Chem. Phys. **72**, 1071 (1980)
83. P. Esherick, A. Owyoung, C.W. Patterson, J. Phys. Chem. **87**, 602 (1983)
84. J.E. Lolck, A. Owyoung, P. Esherick, J. Raman Spectrosc. **16**, 163 (1985)
85. G. Millot, B. Lavorel, R. Chaux, R. Saint-Loup, G. Pierre, H. Berger, J.I. Steinfeld, B. Foy, J. Mol. Spectrosc. **127**, 156 (1988)
86. L.S. Rothman, D. Jacquemart, A. Barbe, D. Chris Benner, M. Birk, L.R. Brown, M.R. Carleer, C. Chackerian Jr., K. Chance, L.H. Coudert, V. Dana, V.M. Devi, J.-M. Flaud, R.R. Gamache, A. Goldman, J.-M. Hartmann, K.W. Jucks, A.G. Maki, J.-Y. Mandin, S.T. Massie, J. Orphal, A. Perrin, C.P. Rinsland, M.A.H. Smith, J. Tennyson, R.N. Tolchenov, R.A. Toth, J. Vander Auwera, P. Varanasi, G. Wagner, J. Quant. Spectrosc. Radiat. Transfer **96**, 139 (2005)
87. L.R. Brown, J. Quant. Spectrosc. Radiat. Transfer **96**, 251 (2005)
88. Y. He, B.J. Orr, Appl. Phys. B **79**, 941 (2004)
89. Y. He, B.J. Orr, Appl. Opt. **44**, 6752 (2005)
90. J.D. Berger, A. Anthon, Optics Photonics News **March 2003**, 42 (2003)
91. L.-H. Deng, X.-M. Gao, Z.-S. Cao, W.-D. Chen, W.-J. Zhang, Z.-B. Gong, J. Quant. Spectrosc. Radiat. Transfer **103**, 402 (2007)
92. A.W. Liu, S. Kassi, A. Campargue, Chem. Phys. Lett. **447**, 16 (2007)
93. D.C. Hanna, D.J. Pointer, D.J. Pratt, IEEE J. Quantum Electron. **QE-22**, 332 (1986)
94. Y. Taira, K. Ide, H. Takuma, Chem. Phys. Lett. **91**, 299 (1982)
95. R.B. Lopert, Measured stimulated Raman gain in methane. Ph.D. Thesis, University of California, Irvine, 1983
96. J.-E. Lolck, A.G. Robiette, Chem. Phys. Lett. **64**, 195–199 (1979)
97. J.-E. Lolck, A.G. Robiette, J. Mol. Spectrosc. **88**, 14 (1981)
98. J.-E. Lolck, A.G. Robiette, L.R. Brown, R.H. Hunt, J. Mol. Spectrosc. **92**, 229 (1982)
99. G. Poussigue, E. Pascaud, J.P. Champion, G. Pierre, J. Mol. Spectrosc. **93**, 351 (1982)
100. T.F. Johnston, W. Proffitt, IEEE J. Quantum Electron. **QE-16**, 483 (1980)
101. A.A. Kaminskii, H.J. Eichler, P. Reiche, R. Uecker, Laser Phys. Lett. **2**, 489 (2005)
102. E.A. Khazanov, Quantum Electron. **31**, 351 (2001)
103. E. Khazanov, A. Anastasiyev, N. Andreev, A. Voytovich, O. Palashov, Appl. Opt. **41**, 2947 (2002)
104. W.A. Clarkson, N.S. Felgate, D.C. Hanna, Opt. Lett. **24**, 820 (1999)
105. R. Hua, S. Wada, H. Tashiro, Opt. Commun. **175**, 189 (2000)
106. R. Kandasamy, M. Yamanaka, Y. Izawa, S. Nakui, Opt. Rev. **7**, 149 (2000)
107. K. Levenberg, Q. Appl. Math. **2**, 164–168 (1944)
108. D.W. Marquardt, J. Soc. Appl. Math. (SIAM J.) **11**, 431 (1963)
109. H. Naus, I.H.M. van Stokkum, W. Hogervorst, W. Ubachs, Appl. Opt. **40**, 4416 (2001)
110. A. Savitzky, M.J.E. Golay, Anal. Chem. **36**, 1627 (1964)
111. J. Steinier, Y. Termonia, J. Deltour, Anal. Chem. **44**, 1906 (1972)
112. H.H. Madden, Anal. Chem. **50**, 1383 (1978)
113. L.A. Rahn, R.L. Farrow, M.L. Koszykowski, P.L. Mattern, Phys. Rev. Lett. **45**, 620 (1980)
114. M. Péalat, M. Lefebvre, J.-P.E. Taran, P.L. Kelley, Phys. Rev. A **38**, 1948 (1988)
115. A. Weber, High-resolution rotational Raman spectra of gases, in *Raman Spectroscopy of Gases and Liquids*, ed. by A. Weber. Topics in Current Physics Series, vol. 11 (Springer, Berlin, 1979), pp. 71–121, Chap. 3